

Review

Nanomaterial-based CT contrast agents and their applications in image-guided therapy

Zeyu Jiang^{1,3*}, Meihua Zhang^{2*}, Peifeng Li¹✉, Yin Wang^{1,2}✉, Qinrui Fu^{1,2}✉

1. Institute for Translational Medicine, The Affiliated Hospital of Qingdao University, College of Medicine, Qingdao University, Qingdao 266021, China.
2. Key Laboratory of Birth Regulation and Control Technology of National Health Commission of China, Maternal and Child Health Care Hospital of Shandong Province affiliated to Qingdao University, Jinan, 250014, China.
3. Department of Cardiovascular Medicine, The Affiliated Hospital of Qingdao University, College of Medicine, Qingdao University, Qingdao 266021, China.

*These authors contributed equally to this work.

✉ Corresponding authors: E-mail: peifli@hotmail.com; wangyin@sibs.ac.cn; fuqinrui2018@163.com.

© The author(s). This is an open access article distributed under the terms of the Creative Commons Attribution License (<https://creativecommons.org/licenses/by/4.0/>). See <http://ivyspring.com/terms> for full terms and conditions.

Received: 2022.10.07; Accepted: 2022.12.01; Published: 2023.01.01

Abstract

Computed tomography (CT), a diagnostic tool with clinical application, comprehensive coverage, and low cost, is used in hospitals worldwide. However, CT imaging fails to distinguish soft tissues from normal organs and tumors because their mass attenuation coefficients are similar. Various CT contrast agents have been developed in recent years to improve the sensitivity and contrast of imaging. Here, we review the progress of nanomaterial-based CT contrast agents and their applications in image-guided therapy. The CT contrast agents are classified according to their components; gold (Au)-based, bismuth (Bi)-based, lanthanide (Ln)-based, and transition metal (TM)-based nanomaterials are discussed. CT image-guided therapy of diseases, including photothermal therapy (PPT), photodynamic therapy (PDT), chemotherapy, radiotherapy (RT), gas therapy, sonodynamic therapy (SDT), immunotherapy, starvation therapy, gene therapy (GT), and microwave thermal therapy (MWTT), are reviewed. Finally, the perspectives on the CT contrast agents and their biomedical applications are discussed.

Key words: material science, contrast agent, CT imaging, diagnosis, therapy

Introduction

X-ray computed tomography (CT) is one of the most widely and commonly used non-invasive clinical imaging modalities owing to its high efficiency, low cost, and easy access [1]. The CT scanner was developed by Godfrey Hounsfield at Electric and Musical Industries (EMI) LTD, and the first clinical trial was performed using a prototype CT scanner (Mark I) in 1972 [2]. CT imaging can precisely display human tissues and organs, significantly advancing diagnostics. Therefore, Godfrey Hounsfield was awarded the Nobel Prize in Medicine in 1979, and the CT unit was named Hounsfield unit (HU) after him to honor his contribution to science [3].

When an X-ray beam traverses a patient's body, it is attenuated by absorption or deflection [4]. The detectors, located on opposite sides of the patient, collect the attenuated X-rays, which are then

converted and computerized to obtain images [5]. This X-ray attenuation (mass attenuation coefficient) is related to the atomic number (Z) and K-shell absorption edge (K-edge) energy (*i.e.*, the energy required to eject an inner K-shell electron) of the elements in tissues or contrast agents [6]. When an X-ray beam passes through a human body, tissues with different attenuation coefficients can be distinguished and presented on CT images. The inherent contrast between the bone and surrounding tissues is large enough to distinguish them. However, since most soft tissues, such as normal organs and tumors, have similar mass decay coefficients, it is difficult to distinguish subtle changes in soft tissues. To address this challenge, exogenous CT contrast agents with additional X-ray attenuation have been introduced at lesion sites to distinguish soft tissues,

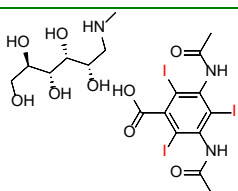
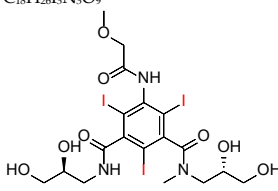
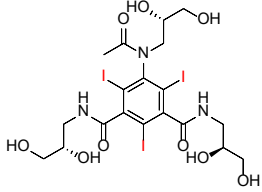
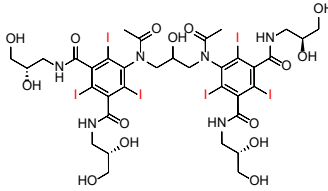
such as normal organs and tumors [7]. Currently, commercially available CT contrast agents for *in vivo* imaging are composed of iodinated small molecules, including meglumine diatrizoate, iopromide, iohexol, and iodixanol (Table 1) [8]. However, the iodinated contrast agents suffer from several limitations: (1) small atomic number and low K-edge energy resulting in a low contrast efficiency, (2) limited applicable population due to its allergic reaction and nephrotoxicity, and (3) non-specific biodistribution requiring high concentrations to improve contrast. Therefore, developing CT contrast agents with superior efficiency, safety, and excellent targeting has become an urgent and challenging task to improve the contrast effect of CT imaging.

Nanotechnology, a transformative technology with the potential to stimulate scientific innovation while greatly benefiting society, has come a long way in the last few decades. Various nanomaterials have been developed as promising agents for biomedical applications due to their unique physical and chemical properties, such as controllable synthesis

and easy surface modification [9, 10]. Among the diverse development of nanomaterials, metal-based inorganic nanoparticles (NPs) with high atomic numbers and large X-ray attenuation coefficients show great potential for achieving specific bioimaging as CT contrast agents [11]. To date, many contrast agents for CT imaging have been reported, including gold (Au)-based nanomaterials, bismuth (Bi)-based nanomaterials, lanthanide (Ln)-based nanomaterials, transition metal (TM)-based nanomaterials, among others.

The separation of diagnosis and treatment is one of the main challenges in the clinic. Advanced nanomaterials with integrated diagnostic and therapeutic capabilities can provide direct evidence of an early diagnosis, development, and progression of the disease, enabling real-time imaging of drugs for disease detection and image-guided treatment. Therefore, multifunctional nanomaterials with integrated diagnostic and therapeutic properties have emerged as a research hot spot.

Table 1. Commercial CT contrast agents and their properties

Common name	Commercial name	Properties	Molecular formula	Advantages	Disadvantages
Meglumine diatrizoate	Angiografan®	Ionic monomers (hyperosmolality)	 $C_{18}H_{26}I_2N_5O_9$	Low cost, applications in ureterography and salpingography.	Anaphylaxis, nephrotoxicity, and local stimulation not recommended for angiography
Iopromide	Ultravist®	Nonionic monomers (secondary hyperosmolality)	 $C_{18}H_{24}I_2N_5O_8$	High solubility and hydrophilicity, permission for angiography.	Nephrotoxicity, lactic acidosis
Iohexol	Omnipaque®	Nonionic monomers (secondary hyperosmolality)	 $C_{19}H_{26}I_2N_5O_9$	Low viscosity and high safety, permission for myelography and ventriculography.	Anaphylaxis, nephrotoxicity
Iodixanol	Visipaque®	Nonionic dimer (isoosmolality)	 $C_{38}H_{44}I_4N_{10}O_{15}$	Minimal nephrotoxicity, applicable to patients with renal insufficiency.	High cost

Here, we focus on the development of nanomaterial-based CT contrast agents and their biomedical applications in recent years (**Figure 1**). First, we offer a comprehensive outline of the available CT contrast agents, including Au-based, Bi-based, Ln-based, and TM-based nanomaterials. Particular attention has been paid to the synthesis methods and imaging capabilities of these contrast agents. We then address recent developments in CT image-guided therapy, including photothermal therapy (PPT), photodynamic therapy (PDT), chemotherapy, radiotherapy (RT), gas therapy, sonodynamic therapy (SDT), immunotherapy, starvation therapy, gene therapy (GT), and microwave thermal therapy (MWT). Challenges, opportunities, and future research priorities are then discussed.

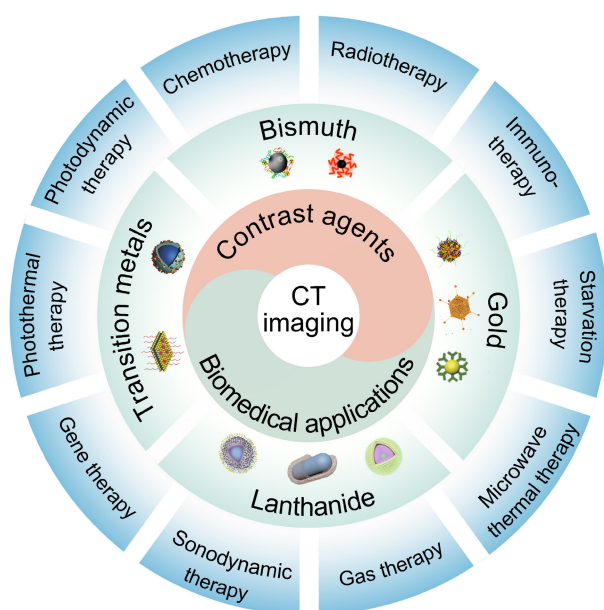


Figure 1. Schematic illustration of nanomaterial-based CT contrast agents and CT image-guided therapies.

Nanomaterial-based CT contrast agents

Gold nanoparticles

Iodinated CT contrast agents, widely used in clinical diagnosis, are rapidly excreted through the kidney, resulting in a short imaging time and nephrotoxicity. In addition, iodinated contrast agents are distributed nonspecifically throughout the intravascular and extravascular space, resulting in ambiguous CT images [12]. Gold nanoparticles (AuNPs), with high X-ray attenuation and K-edge energy (80.7 keV), can provide higher imaging contrast at high X-ray tube voltages than iodinated CT contrast agents at the same concentration [8]. AuNPs also allow facile surface modifications to increase

their biocompatibility and durability due to their high affinity for thiol derivatives [13]. Furthermore, AuNPs with controllable shapes have been synthesized as nanospheres [14, 15], nanorods [16–19], nanostars [20–22], nanoplates [23], nanocages [24], nanoshells [25], nanoprisms [26], and nanodisks [27]. These AuNPs with unique chemical, electrical, and optical properties have been widely used in the biomedical field.

It has been shown that the AuNP size does not affect the X-ray attenuation at the same concentration [28, 29]. But an enhanced *in vivo* CT imaging signal can be achieved by increasing local intratumoral concentrations that can be achieved by designing appropriately sized particles to aggregate into the region of interest [29, 30]. For example, Dong *et al.* synthesized six PEGylated gold nanospheres (AuNSps) with different sizes in the range of 4–152 nm and evaluated their CT contrast properties *via* clinical CT scanners (**Figure 2A**) [29]. The results showed that small AuNSps (4 nm and 15 nm) produced more long-lasting and stronger CT contrast than large ones in the blood vessels as they were not easy to be recognized and cleared by the mononuclear phagocyte system when passing through the liver and kidney, resulting in a high concentration of AuNSps enriched in the blood pool [31]. Conversely, large AuNSps (>50 nm) were easily deposited in the liver and spleen, offering outstanding CT contrast of the liver and spleen region.

Although the CT contrast effect *in vitro* is not substantially affected by the shape of NPs, the gold nanorods (AuNRs) exhibit a stronger *in vivo* CT contrast due to better performance in evading clearance by phagocytes and attaining a longer circulation time and higher intratumoral enrichment than AuNSp [16–19]. Liang *et al.* developed Arg-Gly-Asp (RGD)-modified AuNR nanoprobe with no toxicity, high contrast, and long imaging time as promising contrast agents for *in vivo* CT imaging (**Figure 2B**) [32]. Also, gold nanostars (AuNSs) with multiple sharp branches can be modified with polydopamine-targeting peptide to improve CT contrast due to the greater surface area and extended serum half-life, achieving much longer intravascular signal stability (**Figure 2C**) [20–22]. Moreover, Lu *et al.* developed a P75 (a novel EGFR-targeting peptide)-modified triangular gold nanoplates (AuNPTs-PEG-P75) that could target overexpressed epidermal growth factor receptor (EGFR) in non-small cell lung cancer to realize specific CT imaging *in vivo* (**Figure 2D**) [23].

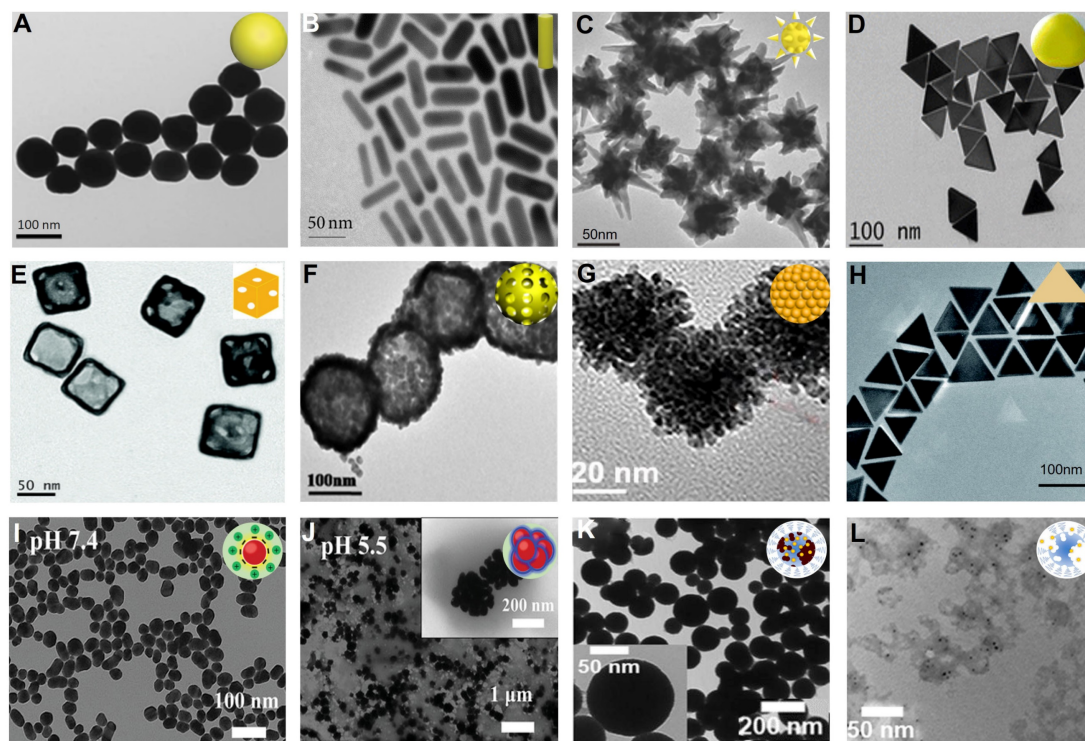


Figure 2. Gold-based NPs. TEM images of (A) gold nanospheres, (B) gold nanorods, (C) gold nanostars, (D) gold nanoplates, (E) gold nanocages, (F) gold nanoshells, (G) Au₂Pt NPs, (H) Gd-Au NPrs, (I) CPP-PSD@Au at pH 7.4, (J) CPP-PSD@Au at pH 5.5, (K) PPB NPs, (L) PPB NPs in 10 mM H₂O₂. (A) Adapted with permission from [29], Copyright 2019 Springer Nature. (B) Adapted with permission from [32], Copyright 2016 Hindawi Publishing Corporation. (C) Adapted with permission from [22], Copyright 2016 Wiley-VCH. (D) Adapted with permission from [23], Copyright 2018 American Chemical Society. (E) Adapted with permission from [24], Copyright 2018 The Royal Society of Chemistry. (F) Adapted with permission from [25], Copyright 2017 American Chemical Society. (G) Adapted with permission from [43], Copyright 2020 Elsevier. (H) Adapted with permission from [26], Copyright 2017 The Royal Society of Chemistry. (I–J) Adapted with permission from [48], Copyright 2021 Wiley-VCH. (K–L) Adapted with permission from [49], Copyright 2019 American Chemical Society.

Theranostic agents represent an emerging method to meet clinical needs by combining diagnostic and therapeutic modalities into one specific system. As inorganic nanoscale carriers, gold nanocages (AuNCs) with hollow structures and gold nanoshells (AuNShs) with porous walls have been investigated as theranostic agents over the past few years [33–35]. The surfaces of AuNCs and AuNShs can be easily modified by Au–S bonding with various molecules and ligands, making them promising drug delivery vehicles and CT contrast agents [36, 37]. Hu *et al.* developed AuNC theranostic agents by integrating a CT contrast agent, doxorubicin (DOX), and miR-122 (a liver-specific miRNA) into a single system for achieving CT image-guided enhanced cancer therapy by combining chemotherapy and gene therapy (Figure 2E) [24]. Li *et al.* designed bovine serum albumin (BSA)-coated hollow AuNShs as a multifunctional drug delivery platform to achieve CT image-guided drug delivery (Figure 2F) [25].

Despite the advantages of CT imaging in spatial resolution, accurate differentiation of different tissue densities remains a challenge. The use of multimodal imaging contrast agents is a promising avenue for future innovations in biomedical research, which can help overcome the inadequacies of a single CT imaging modality, achieve complementary

advantages, and broaden the range of applications of molecular imaging techniques [38–41]. As one of the noble metal NPs, AuNPs possess excellent light absorption and photoacoustic (PA) imaging capability due to the localized surface plasmon resonance (LSPR) effect [42]. Thus, Xing *et al.* fabricated a bimetallic nanoplatform (Au₂Pt NPs) with strong absorption in the NIR region and high X-ray attenuation with excellent CT/PA dual-modal imaging capability (Figure 2G) [43]. The CT value at the tumor site increased from 19.06 Hu to 489.35 HU 12 h after injection, and a strong PA signal could be observed, improving the diagnostic ability by combining the PA and CT imaging. The introduction of magnetic resonance imaging (MRI) can effectively compensate for the limitation of CT imaging in distinguishing soft tissues [44–46]. Lu *et al.* prepared multifunctional gadopentetic acid-decorated gold nanoprisms (Gd-AuNPrs), in which gadolinium with excellent magnetic properties and AuNPs with high X-ray attenuation were used for T₁-weighted MRI and CT imaging, respectively (Figure 2H) [26]. The longitudinal relaxivity (r₁) of Gd-AuNPrs was 23.1 mM⁻¹ s⁻¹, and its X-ray absorption coefficient was 959.3 HU L g⁻¹; hence the Gd-AuNPrs could be used as promising dual-modal imaging contrast agents.

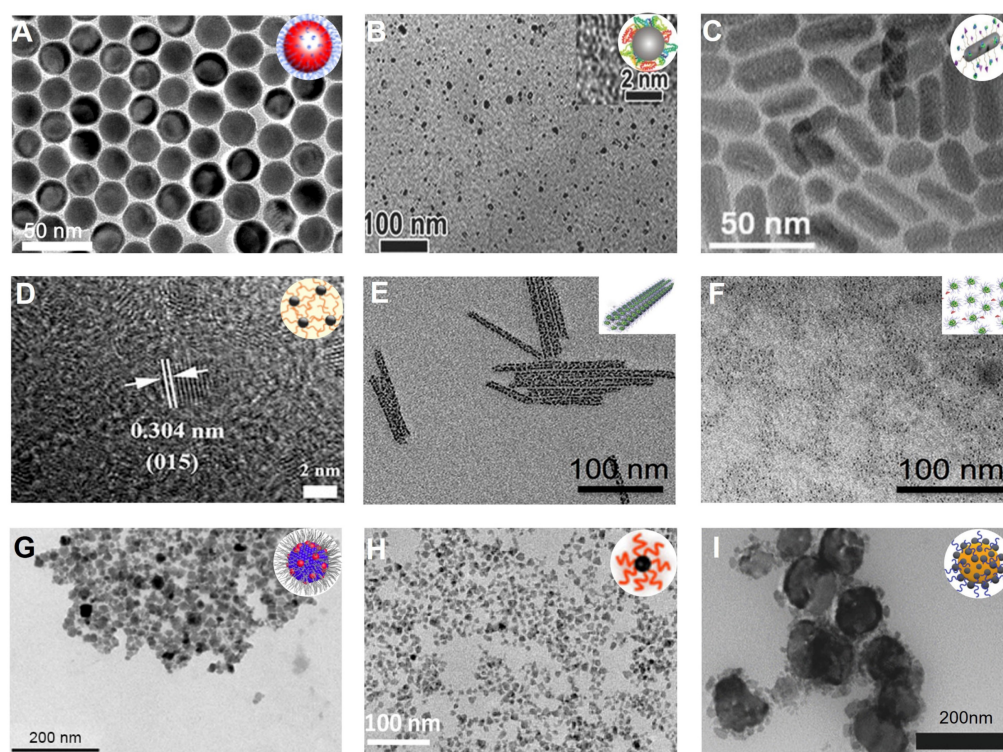


Figure 3. Bismuth-based NPs. TEM images of (A) BiNPs, (B) Bi_2S_3 NPs, (C) Bi_2S_3 nanorods, (D) Bi_2Se_3 nanodots, (E) $(\text{BiO})_2\text{CO}_3$ nanotubes, (F) $(\text{BiO})_2\text{CO}_3$ nanoclusters, (G) HA- Bi_2O_3 NPs, (H) Cu_3BiS_3 NDs, (I) $\text{BiOI}@\text{Bi}_2\text{S}_3$ NPs. (A) Adapted with permission from [54], Copyright 2016 American Chemical Society. (B) Adapted with permission from [58], Copyright 2016 Wiley-VCH. (C) Adapted with permission from [59], Copyright 2019 Wiley-VCH. (D) Adapted with permission from [62], Copyright 2021 Frontiers Media S.A. (E-F) Adapted with permission from [63], Copyright 2018 American Chemical Society. (G) Adapted with permission from [64], Copyright 2017 Dove Press Ltd. (H) Adapted with permission from [65], Copyright 2016 American Chemical Society. (I) Adapted with permission from [66], Copyright 2017 Wiley-VCH.

Tumor microenvironment (TME) such as pH, hypoxia, and H_2O_2 -responsive assembly of NPs can improve the accumulation of contrast agents in tumors, achieving enhanced CT contrast [47]. Zhang *et al.* developed a pH-sensitive Au-based nanotracer (CPP-PSD@Au) that was sequentially modified with the pH-sensitive polymer polysulfonamide (PSD) and cell-penetrating peptide (CPP) for enhanced labeling and long-term tracking of CT imaging of stem cells in pulmonary fibrosis treatment (Figure 2I-J) [48]. Once the nanotracer entered the cell, the CPP was shed from the surface of the CPP-PSD@Au in the endosome, causing the monodisperse CPP-PSD@Au to rapidly aggregate into agglomerates due to the PSD protonation in the acidic environment, thereby significantly increasing intracellular retention for enhanced CT imaging contrast. However, large nanocomposites are not readily metabolized in the cells, which may lead to increased cytotoxicity. Thus, Cormode *et al.* developed H_2O_2 -responsive CT and PA dual-mode contrast agents using the AuNP payload in an arylboronate polyphosphazene derivative (PPB) core (Figure 2K) [49]. PPB was efficiently degraded in the TME with overexpression of H_2O_2 , which triggered a switch-off of the PA signal and a slight reduction in the CT signal, causing a concentration reduction of local AuNPs (Figure 2L) [50]. This

H_2O_2 -triggered degradation of the nanoprobe led to a significant increase in the CT/PA contrast ratio, allowing ratiometric imaging to identify reactive oxygen species (ROS) overexpression.

Bismuth-based nanoparticles

Bismuth (Bi) possesses a higher atomic number (Bi: 83, Au: 79) and larger X-ray attenuation coefficient (Bi: $5.74 \text{ cm}^2/\text{g}$, Au: $5.16 \text{ cm}^2/\text{g}$, at 100 keV) than Au, and is a promising CT contrast agent for diagnosis of diseases [51]. As a noble metal, the high cost of Au inevitably limits its applications in clinical practice. However, Bi is a relatively cheap and low-toxic heavy metal and has been used as a pharmaceutical ingredient to treat various diseases, such as gastritis, dyspepsia, ulcers, and infections [52]. Bi nanoparticles (BiNPs) can improve the X-ray absorption efficiency and address the bottleneck of CT imaging contrast agents in terms of sensitivity [53]. Wei *et al.* synthesized dodecanethiol-modified BiNP contrast agents for CT imaging of the gastrointestinal tract (GIT) (Figure 3A); the CT contrast enhancement of the BiNP contrast agents was 1.5-fold higher than BaSO_4 , a traditional clinical CT contrast agent for the diagnosis of GIT [54].

Bi-based chalcogenides are also commonly used as CT contrast agents in clinical use due to their stable chemical properties [55]. In 2006, Rabin and

coworkers developed polyvinylpyrrolidone (PVP)-coated bismuth sulfide (Bi_2S_3) nanocrystals as an injectable CT contrast agent [56], which possessed higher stability and X-ray attenuation coefficient (5-fold higher than an iodinated contrast agent), longer circulation times *in vivo* (140 ± 15 min), and more reliable security than iodinated CT contrast agents. The lymph nodes could be distinctly observed, and the CT signal intensity in the liver region increased from -22 ± 77 HU to 740 ± 210 HU at 24 h post-administration, indicating that Bi_2S_3 NPs could be used as an excellent CT contrast agent for diagnosis of diseases.

Besides the X-ray attenuation coefficient, the circulation half-life is one of the essential parameters that must be considered to improve the CT imaging capability of Bi-based contrast agents. In this context, modification with biocompatible materials may improve the circulating half-life of Bi-based contrast agents. For example, the circulation half-life of Pluronic F127-modified Bi_2S_3 NPs could be extended to 5 h, demonstrating excellent CT contrast capability *in vivo* [57]. Chai *et al.* prepared BSA-modified Bi_2S_3 contrast agent with high circulation half-life (14.85 h), X-ray attenuation, and 6-fold higher CT imaging capability than iobitridol (**Figure 3B**) [58]. Prolonging the half-life of contrast agents in tumor cells has prominent clinical significance. Zhang *et al.* prepared CPP-modified Bi_2S_3 nanorods (NRs) CT contrast agent (BPZP) by a solvothermal method to extend the contrast effect at the tumor site (**Figure 3C**) [59]. The 4T1 tumor-bearing mice were given BPZP intravenously, and the CT signals at the tumor site were observed at 2 h post-injection and maintained at 12 h post-injection, which was attributed to the persistent escape of BPZP under CPP action.

Targeted imaging is also an effective method to enhance the imaging capabilities of specific organs, especially tumors. Zhou *et al.* prepared folate-modified perfluorohexane (PFH) NPs to carry Bi_2S_3 nanodots for targeted CT imaging of the tumor [60]. After intravenous administration, the CT values of tumors in the targeted group (251 HU) was enhanced compared with the non-targeted group (33 HU) due to the excellent ability of folate to target tumors. Moreover, Kinsella *et al.* developed a nine-amino acid cyclic peptide (LyP-1, CGNKRTRGC)-labeled Bi_2S_3 NPs for CT imaging of 4T1 tumors [61]. The LyP-1 labeled Bi_2S_3 NPs preferentially accumulated in the tumor region ($8.4 \pm 2.1\%$ injected dose per gram of tissue) relative to unlabeled NPs ($3.2 \pm 1.7\%$ injected dose per gram of tissue) due to excellent targeting ability of LyP-1 for 4T1 cells, thus enabling acquisition of high-fidelity CT images of the tumor.

Apart from Bi_2S_3 NPs, other Bi-based nano-

materials, such as bismuth selenide (Bi_2Se_3), bismuth oxide (Bi_2O_3), bismuth oxyiodide (BiOI), bismuth oxychloride (BiOCl), and Cu_3BiS_3 , could also be used as excellent CT contrast agents. Yuan *et al.* synthesized ultrasmall polyethylenimine (PEI)-decorated Bi_2Se_3 (PEI- Bi_2Se_3) nanodots *via* a facile room temperature method for CT imaging of cancer (**Figure 3D**) [62]. The CT contrast of PEI- Bi_2Se_3 nanodots in the tumor region was twice as high as that of iobitridol at equivalent concentrations.

Ultrasmall-sized nanomaterials avoid potential toxicity due to their rapid renal clearance but are not effective for tumor targeting and CT imaging. To solve this contradiction, Ling *et al.* prepared bismuth subcarbonate ($(\text{BiO})_2\text{CO}_3$) nanotubes (BNTs) with approximately 100 nm in length and 8 nm in diameter by assembling 1.5 nm ultrasmall $(\text{BiO})_2\text{CO}_3$ nanoclusters (BNCs) (**Figure 3E**) [63]. The blood-clearance half-life of the BNTs were 26.99 ± 0.41 h, which was about 7-fold longer than that of the BNCs (3.77 ± 1.53 h), suggesting that the BNT contrast agents offered the tumor accumulation ability to enhance CT imaging capability. Furthermore, after localization in the tumor tissue, BNTs could be disassembled into nanoclusters in an acidic TME (**Figure 3F**), providing BNTs a superior degradation capability.

To avoid the biotoxicity caused by the intrinsic potential accumulation of sulfur element, Wu *et al.* prepared hyaluronic acid (HA)-functionalized bismuth oxide NPs (HA- Bi_2O_3 NPs) *via* one-pot hydrothermal method for targeted CT imaging of the tumor (**Figure 3G**) [64]. In VSMC, SMMC-7721, and MCF7 cells, the HA- Bi_2O_3 NPs exhibited negligible cytotoxicity at different concentrations. HA- Bi_2O_3 NPs could be specifically absorbed in cancer cells overexpressing CD44 receptors, and strong targeted CT imaging capabilities were observed. The CT value at the tumor site increased from 60 HU to approximately 200 HU 10 min after the injection.

Limited by the poor sensitivity of CT imaging in soft tissues, a high concentration of the contrast agent is usually required to achieve the imaging effect in the clinic [39]. Due to the complementary advantages, dual-modal imaging is a good strategy for solving the issues. For example, CT imaging gives structural details of deep tissues, while PA imaging provides high sensitivity to soft tissues [40]. Bimetallic sulfide-based hybrid nanoparticles have been developed for CT/PA imaging due to their unique optical properties. Chen *et al.* prepared the single-phased ternary bimetal sulfide nanomaterial, Cu_3BiS_3 NDs, with inherent high X-ray attenuation and strong NIR absorption coefficient ($>10^5 \text{ cm}^{-1}$) for CT/PA dual-modal imaging (**Figure 3H**) [65]. When

Cu_3BiS_3 NDs were intravenously injected into 4T1 tumor-bearing mice at a low concentration (200 μL , 10 mg/mL), CT/PA signals of tumor were observed at 2 h post-injection and lasted for up to 24 h, indicating the excellent imaging effect of Cu_3BiS_3 NDs in the tumor region. Zhao *et al.* synthesized semiconductor heterojunction $\text{BiOI@Bi}_2\text{S}_3$ NPs (SHNPs) *via* the hydrothermal procedure and anion exchange method as a dual-modal contrast agent for CT/PA imaging (**Figure 3I**) [66]. The $\text{BiOI@Bi}_2\text{S}_3$ heterojunction improved the absorption in the NIR window and enhanced the X-ray attenuation due to the iodine element doping. At the same concentration, SHNPs showed a higher CT signal than iopromide, while PA signals of SHNPs were also observed at very low concentrations, demonstrating the promising potential of SHNPs in CT/PA imaging.

Lanthanide-based nanoparticles

Lanthanide (Ln) elements exhibit higher X-ray attenuation coefficients than iodine elements [67], and their K-edge energy is close to the average energies (80-120 keV) of other contrast agents used in CT imaging and can be used as CT contrast agents [12]. Ln elements with atomic numbers ranging from 57 to 71 include Lanthanum (La), Cerium (Ce), Praseodymium (Pr), Neodymium (Nd), Promethium (Pm), Samarium (Sm), Europium (Eu), Gadolinium

(Gd), Terbium (Tb), Dysprosium (Dy), Holmium (Ho), Erbium (Er), Thulium (Tm), Ytterbium (Yb), and Lutetium (Lu).

The chemical properties of metallic oxide NPs are more stable under biological and atmospheric conditions than metallic NPs and are, therefore, more suitable for biomedical applications. Lanthanide oxide (Ln_2O_3) NPs are excellent CT contrast agents because of their high X-ray attenuation energy [68, 69]. Lee *et al.* synthesized polyacrylic acid (PAA)-coated ultrasmall Gd_2O_3 NPs (Gd, Z = 64) by the one-pot polyol method and investigated their X-ray attenuation properties (**Figure 4A**) [68]. The X-ray attenuation rate of Gd_2O_3 NPs was roughly estimated to be 5.9 HU/mM, which was higher than that of Ultravist (4.40 HU/mM). PAA-coated ultrasmall Gd_2O_3 NPs intravenously injected into mice showed that a low injection dose of Gd (~ 0.015 mmol) could produce a better contrast effect than Ultravist (> 0.1 mmol). Atabaev *et al.* prepared PEI-coated Eu_2O_3 (Eu, Z = 63) CT contrast agents using urea homogeneous precipitation protocols (**Figure 4B**) [70]. The CT value of 8 HU/mM per 1 mM metal concentration for $\text{PEI@Eu}_2\text{O}_3$ was significantly higher than $\text{PAA-Gd}_2\text{O}_3$ NPs due to the higher Ln content of the urea homogeneous precipitation protocol compared to the one-pot polyol method.

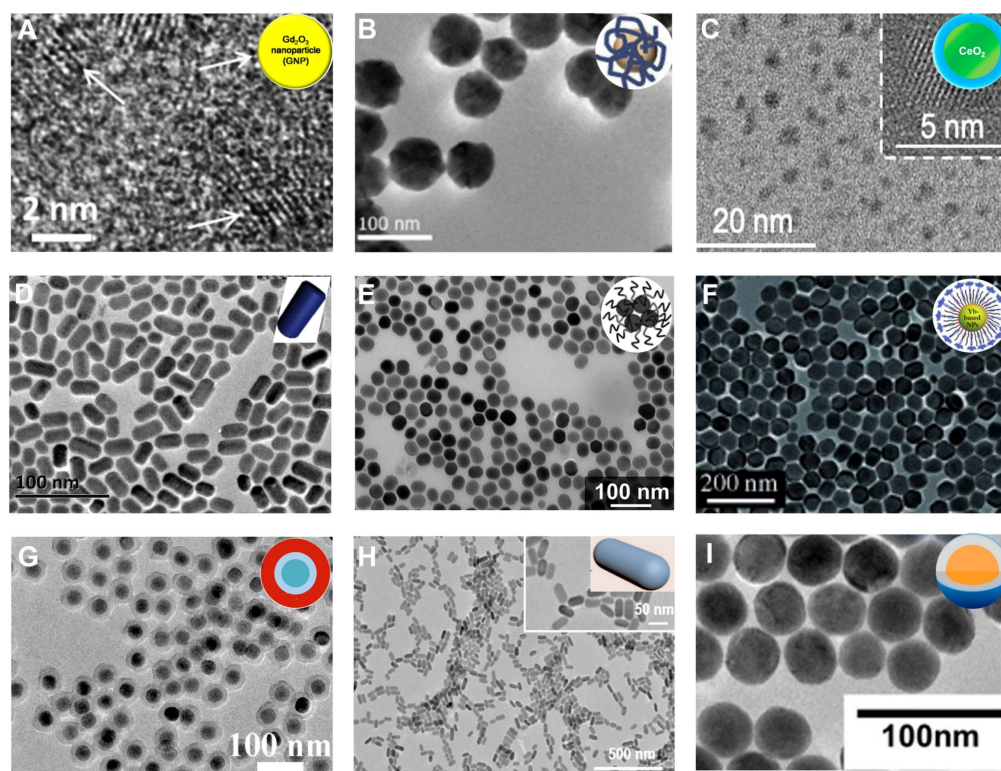


Figure 4. Lanthanide-based NPs. TEM of (A) Gd_2O_3 NPs, (B) Eu_2O_3 NPs, (C) CeO_2 NPs, (D) NaHoF_4 NPs, (E) NaErF_4 NPs, (F) NaYbF_4 NPs, (G) $\text{NaYF}_4:\text{Nd}^{3+}@\text{NaLuF}_4$ NPs, (H) $\text{NaCeF}_4:\text{Gd,Tb ScNPs}$, (I) Yb/Er@Lu@Gd NPs. (A) Adapted with permission from [68], Copyright 2019 Elsevier. (B) Adapted with permission from [70], Copyright 2021 IOP Publishing. (C) Adapted with permission from [72], Copyright 2020 American Chemical Society. (D) Adapted with permission from [74], Copyright 2015 Elsevier. (E) Adapted with permission from [76], Copyright 2018 American Chemical Society. (F) Adapted with permission from [78], Copyright 2012 Wiley-VCH. (G) Adapted with permission from [83], Copyright 2017 American Chemical Society. (H) Adapted with permission from [85], Copyright 2020 American Chemical Society. (I) Adapted with permission from [86], Copyright 2017 American Chemical Society.

Besides Gd_2O_3 and Eu_2O_3 , Cerium oxide (CeO_2) NPs could also serve as an alternative for CT contrast agents. Cerium (Ce, $Z = 58$) has a K-edge energy at 40.4 keV that is slightly higher than the iodine element (33.2 keV), matches well with the X-ray beams used in CT imaging, and can produce strong CT contrast [71]. Using a precipitation method, Cormode *et al.* prepared a Ce-based CT contrast agent (Dex-CeNP) consisting of dextran-coated CeO_2 NPs for GIT imaging (**Figure 4C**) [72]. Dex-CeNPs provided comparable or slightly better CT contrast than iopamidol 60 min after oral administration to healthy mice, demonstrating its potential for GIT imaging. However, when DSS-induced colitis mice received Dex-CeNPs, the CT values of the large intestine significantly increased (about 50 times) compared to iopamidol due to the affinity of dextran for inflammatory sites. Also, Dex-CeNPs neutralized free radicals from ionizing radiation while protecting against oxidative damage, which was beneficial in preventing oxidative damage caused by CT examination.

Lanthanide Fluoride ($NaLnF_4$), with significant chemical stability, is an excellent CT contrast agent because it can bundle numerous ions together in the form of stabilized nanoparticles [73]. As heavy rare earth elements, Ho ($Z = 67$), Er ($Z = 68$), and Yb ($Z = 70$) have high X-ray attenuation coefficients and thus can be used as CT contrast agents. For instance, Ho possesses a higher attenuation coefficient ($3.49 \text{ cm}^2/\text{g}$, at 100 keV) and K-edge value (55.6 keV) than iodine, which endows Ho-based NPs with an outstanding CT imaging contrast performance. Shi *et al.* synthesized PEGylated $NaHoF_4$ NPs through the thermal decomposition method for CT imaging (**Figure 4D**) [74]. *In vitro* slope of the CT values of PEG- $NaHoF_4$ NPs was about 42.1 HU L/g, which was considerably higher than iobitridol (16.5 HU L/g) at the standard concentration. Moreover, when $NaHoF_4$ NPs were injected intravenously into murine breast cancer tumor-bearing mice for 2 h, conspicuous brightness in tumor regions was observed by CT imaging, with CT values significantly increased from 36.6 ± 11.1 before injection to 209.8 ± 40.1 after injection, demonstrating the feasibility of $NaHoF_4$ NPs as CT contrast agents for tumor imaging.

Er, another heavy rare earth element with a K-edge at 57.5 keV, provides the necessary contrast for CT imaging and can be used for blood pool imaging [75]. Gillies *et al.* synthesized an oleate-coated $NaErF_4$ NPs as an excellent CT contrast agent *via* nanoprecipitation method for blood pool imaging *in vivo*, providing high contrast between the vessels and surrounding tissues due to their high contrast element loading ($>100 \text{ mg/mL}$) and long circulation times (>1

h) (**Figure 4E**) [76]. CT values of the heart and aorta increased by more than 250 HU compared to pre-injection when the contrast agent was injected intravenously into C57BL/6 male mice. Also, the heart chambers did not appear to change in contrast for up to 60 min.

Similarly, Yb with a higher atomic number ($Z = 70$) and K-edge energy (61 keV) than other Ln elements except for Lu, can be used as a high-performance CT contrast agent for *in vivo* angiography and lymph node mapping [77]. Lu *et al.* developed PEGylated Yb-based contrast agents ($NaYbF_4$ NPs) with negligible cytotoxicity and prolonged circulation time ($>1 \text{ h}$) *in vivo* for CT imaging (**Figure 4F**) [78]. The CT value of $NaYbF_4$ NPs was 115 HU at 120 KVp, which was higher than most metallic contrast agents such as Au-based (65 HU) and Bi-based NPs (85 HU), since the K-edge of Yb was located within a higher energy region of the X-ray spectrum. After intravenous injection, a clear signal enhancement of the large vessels and lymph nodes was observed at 20 min post-injection (from 56.1 HU to 336.5 HU) and sustained for a minimum of 1 h.

Doping of Ln-based NPs can alter the longitudinal or transverse relaxation times and improve the conversion luminescence efficiency of activated ions because of their unique 4f electronic structure. Thus, Ln-based NPs are also used in MRI and optical imaging to remedy the deficiencies of CT imaging [79-82]. Li *et al.* fabricated a polydopamine (PDA)-coated $NaYF_4:Nd^{3+}@NaLuF_4$ nanocomposites using the reverse microemulsion approach for NIR-II optical imaging and CT imaging to provide accurate information on tumors (such as spatial position and anatomical details) (**Figure 4G**) [83]. Due to the high X-ray attenuation coefficient of Lu ($Z = 71$), the slope of the CT values for the $NaYF_4:Nd^{3+}@NaLuF_4$ nanocomposites was approximately 45.23 HU L/g, which was much higher than that for iodixanol (20.37 HU L/g). The luminescent NIR-II signal was captured upon irradiation by an 808 nm laser due to doping neodymium (Nd^{3+}).

After intratumoral injection of $NaYF_4:Nd^{3+}@NaLuF_4$ into HeLa tumor-bearing nude mice, the NIR-II and CT signals were observed at the tumor site, demonstrating its potential as a bimodal probe for tumor imaging. The combination of MRI and CT imaging provides more information on the tumor due to the high resolution of MRI in soft tissues [84]. Yang *et al.* synthesized a Ce-doped $NaCeF_4:Gd,Tb$ scintillating nanoparticle (ScNPs) with uniform rod-like morphology *via* a high-temperature reaction method for CT and MR bimodal imaging (**Figure 4H**) [85]. Because of the participation of Ce^{3+} , Tb^{3+} , and Gd^{3+} ions, the computed CT value slope was 38.152 HU

L/g and the r_2 relaxation was $39.89 \text{ mM}^{-1} \text{ s}^{-1}$, indicating the good performance of ScNPs in CT and T_2 -weighted MR imaging.

Almutairi *et al.* designed $\beta\text{-NaYb}_{0.2}/\text{Er}_{0.8}\text{F}_4@ \text{NaLuF}_4@ \text{NaGdF}_4$ (Yb/Er@Lu@Gd) heteroepitaxial triple-layer core-shell-shell (CSS) NPs as a triple-modal contrast agent for photoluminescence (PL) imaging, MRI, and CT imaging (**Figure 4I**) [86]. The triple-modal contrast agent had many advantages: (1) PL intensity was enhanced from completely quenched state to brightly emissive state at 808 nm irradiation, (2) the r_1 relaxivity of MRI was enhanced by 5-fold from 11.4 to $52.9 \text{ mM}^{-1} \text{ s}^{-1}$ (per Gd^{3+}) at 1.5 T, and (3) the CT value gain was 70 % higher than the iodinated contrast agents at the same mass concentration.

Transition metal-based nanoparticles

Hafnium

Hafnium (Hf) can be used as an excellent CT contrast agent as it has a high atomic number ($Z = 72$), and its K-side energy (65.4 keV) is close to the peak tube potential of clinical CT system (80-120 kVp) [87, 88]. Roeder *et al.* produced roughly spherical and monodispersed PVP functionalized HfO_2 NPs with an adjustable mean diameter of 7-31 nm *via* a sol-gel

method (**Figure 5A**) [89]. The X-ray attenuation of HfO_2 NPs (11.1 HU/mM) at 0.5-50 mM concentration was intermediate between iohexol (6.8 HU/mM) and AuNPs (15.3 HU/mM). HfO_2 and AuNPs exhibited significantly improved CT contrast compared to iohexol due to the Hf and Au K-shell absorption edges at 65.4 and 80.7 keV, respectively. Therefore, HfO_2 can be used as a potential CT contrast agent to provide a better CT contrast effect than iohexol; it is also much cheaper than Au NPs (0.87 USD/g Hf *vs.* 64.06 USD/g Au).

Tantalum

Compared to other transition metals, tantalum (Ta) is a highly biocompatible metal that causes minimal adverse biological reactions in any redox form. Therefore, Ta compounds have been widely employed in clinical implants, artificial joints, stents, and vascular clips for about 50 years [90]. In recent years, Ta has been used as a CT contrast agent due to its high atomic number ($Z = 73$) and K-edge energy (67 keV) in the uppermost energy region of the X-ray spectrum [91]. Hyeon *et al.* prepared uniform-sized tantalum oxide (TaO_x) NPs by a simple microemulsion method (**Figure 5B**) [92]. The CT contrast enhancement of the TaO_x NPs ($4.30 \text{ cm}^2/\text{g}$, at

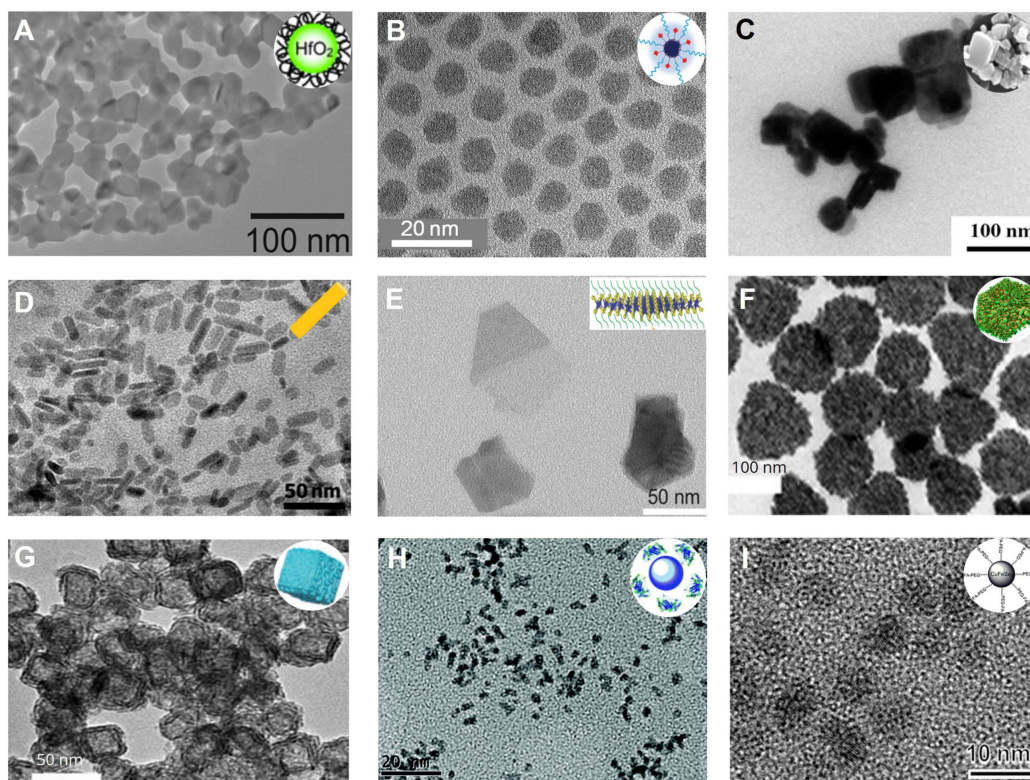


Figure 5. Transition metal-based NPs. TEM images of (A) PVP- HfO_2 NPs, (B) PEG- TaO_x NPs, (C) PCL/PEG-coated WO_3 NPs, (D) PVP-coated Rb_2WO_6 NRs, (E) PVP-capped ReS_2 NSs, (F) IrNPs, (G) Pt Spirals, (H) Pt@BSA NPs, (I) CuFeSe_2 -PEG-FA NPs. (A) Adapted with permission from [89], Copyright 2016 The Royal Society of Chemistry. (B) Adapted with permission from [92], Copyright 2011 American Chemical Society. (C) Adapted with permission from [96], Copyright 2013 Elsevier. (D) Adapted with permission from [97], Copyright 2014 Wiley-VCH. (E) Adapted with permission from [99], Copyright 2018 Wiley-VCH. (F) Adapted with permission from [101], Copyright 2019 American Chemical Society. (G) Adapted with permission from [103], Copyright 2019 Wiley-VCH. (H) Adapted with permission from [104], Copyright 2017 Royal Society of Chemistry. (I) Adapted with permission from [105], Copyright 2021 Dove Press Ltd.

100 keV) was much higher than iodinated CT contrast agents. While TaO_x NPs smaller than 6 nm were cleared from the circulation within seconds after intravenous injection, the larger ones stabilized with PEG had long circulation times (over 3 h) and finally accumulated in the liver and spleen. Therefore, TaO_x NPs are potentially useful for angiography and RES-targeted CT imaging. Shi *et al.* developed biocompatible PEGylated tantalum sulfide (PEG-TaS₂) nanosheets (NSs) by combinatorial grinding and sonication for CT imaging [93]. At 24 h after intravenous administration, the CT values of tumor site increased from 21.3 HU to 44.6 HU. Furthermore, the CT signals in the heart at 2 h post-injection were much brighter than the pre-injection signals, indicating their longer circulation time.

Tungsten

Tungsten (W) is considered an appropriate candidate for CT imaging due to its high atomic number ($Z = 74$) and X-ray absorption coefficient (4.44 cm²/kg, at 100 keV) [94]. However, the toxic nature of the W compound caused death in mice just seconds after intravenous administration [95]. The most likely reason of this toxicity is the aggregation of particles in capillaries and arteries, resulting in embolism and subsequent clogging of blood vessels. To address these issues, Jakhmola *et al.* designed poly- ϵ -caprolactone (PCL) and PEG-modified tungsten oxide (WO₃) NPs for *in vivo* CT imaging (Figure 5C) [96]. The PCL/PEG-coated WO₃ NPs showed good stability under physiological conditions and were non-toxic because the PCL layer inhibited particle agglomeration. The CT value of PCL/PEG-coated WO₃ NPs was approximately 4-fold higher than the iodinated contrast agent (Fenestra VC). Zhao *et al.* reported PVP-coated rhenium tungsten bronze (Rb_xWO₃) NRs for CT imaging (Figure 5D) [97]. The slope of CT values of PVP-coated Rb_xWO₃ NRs was approximately 38.66 HU L/g, much higher than that of Ultravist (13.25 HU L/g), indicating the good contrast efficacy of Rb_xWO₃ NRs for CT imaging. Immediately after the intratumoral injection, the CT signal at the tumor region was visible, demonstrating that Rb_xWO₃ NRs can be employed as an effective contrast agent for *in vivo* CT imaging.

Rhenium

Rhenium (Re) possesses a high Z element ($Z = 75$) and strong X-ray attenuation; hence, Re-based nanomaterials can also serve as an excellent CT contrast agent [98]. Xu *et al.* prepared PVP-capped colloidal rhenium disulfide (ReS₂) NSs with excellent physiological stability and high biocompatibility through a probe sonication-assisted liquid exfoliation

method for *in vivo* CT imaging (Figure 5E) [99]. The ReS₂ NSs showed a superior CT enhancement effect over iopromide, as their X-ray absorption coefficient (20 HU mL/mg) was higher than that of iopromide (15.9 HU mL/mg). After intratumoral injection, the CT values of the tumor region increased from 28.4 to 271.6 HU, indicating that PVP-capped ReS₂ NSs were an excellent CT imaging contrast agent.

Iridium

Iridium (Ir), one of the least abundant noble metal elements with a high atomic number ($Z = 77$) and K-edge energy (71 keV), has attractive physical and chemical properties but has not been studied as a CT contrast agent due to the high price [100]. To overcome the current limitations, Jang *et al.* prepared Ir–Ag–IrO₂ nanoplates (IrNPs) *via* the hydrothermal galvanic replacement-tethered synthetic method for CT imaging (Figure 5F) [101]. The CT value in the tumor region increased from 42.6 HU to 53.2 HU 24 h after intravenous administration, indicating the feasibility of CT imaging to monitor IrNPs accumulation in the tumor.

Platinum

Platinum (Pt), like gold, is another inert noble metal with strong X-ray attenuation and high atomic number ($Z = 78$). Therefore, Pt can potentially be used as a CT contrast agent for disease diagnosis [102]. Zhang *et al.* designed unique PEG-modified hollow Pt spirals with a multilevel structure *via* a simple selective etching strategy (Figure 5G) [103]. Due to its high K-edge energy (78.4 keV), Pt spirals had better contrast than a clinical iodinated CT contrast agent (Omnipaque) at the same concentration (5.39 *vs.* 4.76 HU/mM). A considerable enhancement of CT signals in the tumor region was detected (1.45-fold higher than before injection) 24 h after intravenous injection, showing that the Pt spirals were an excellent CT contrast agent for *in vivo* imaging. In addition, Jia *et al.* fabricated ultrasmall Pt@BSA NPs through a fast albumin-mediated one-pot synthesis method for CT imaging (Figure 5H) [104]. These well-dispersed Pt@BSA NPs with a mean core size of 2.1 nm exhibited excellent colloidal stability, hemocompatibility, and biocompatibility. The CT value of Pt@BSA was approximately 2.4-fold higher than that of Ultravist at the same concentration. The contrast enhancement of the heart was observed (76 ± 4 HU) 5 minutes after intravenous injection of Pt@BSA NPs. However, the contrast enhancement of the heart was not observed 5 minutes after intravenous injection of Ultravist, indicating CT imaging capability of Pt@BSA NPs was superior to current clinical iodinated contrast agents.

Other transition metal-based NPs

It is generally believed that higher atomic numbers imply better X-ray attenuation coefficients and contrast enhancement. However, the transition metal-based NPs (such as Cu, Ag) with atomic numbers less than iodine can also be used as CT contrast agents by increasing local concentration, such as targeted aggregation. Shu *et al.* synthesized CuFeSe₂-PEG-FA NPs with excellent targeting capability for CT imaging (**Figure 5I**) [105]. Upon treatment with the CuFeSe₂-PEG-FA NPs, the CT value (14.1 HU) of 4T1 cells was higher than that of treatment with CuFeSe₂ NPs (1.2 HU) or Ultravist (8.2 HU), because folic acid (FA) targeted the overexpressed FA receptors in malignant tumors. Furthermore, the enrichment concentration of contrast agents *in vivo* could be enhanced by improving their biocompatibility [106]. Wang *et al.* developed spherical, ultrasmall, and monodisperse HA-coated silver NPs (HA-Ag NPs) by the chemical reduction protocol for CT imaging [107]. The HA-Ag NPs exhibited excellent long-term stability, low cytotoxicity, and enhanced CT contrast due to the HA-improved biocompatibility of HA-Ag NPs and facilitated the intratumor enrichment of the contrast agent.

Although commercial iodinated CT contrast agents have been developed from the first generation of ionic monomers to the third generation of non-ionic dimers, their inherent defects are still confusing, such as short blood pool circulation time and nonspecific biodistribution, requiring larger doses of contrast agents to reveal areas of interest. Consequently, AuNPs, with high contrast, easy control of size and surface modifications, controlled half-life, and targeted biodistribution, have attracted intense research in the last two decades. However, the high cost of gold limits its development and use in biomedicine. Bi-based NPs, with better X-ray attenuation properties and lower cost than AuNPs, have been widely used in the biomedical field as a suitable alternative, but encephalopathy and nephropathy caused by their long-term accumulation in the body remain challenging. Lanthanide ions such as Gd³⁺ have been used as commercial MRI contrast agents, indicating their promising potential for clinical applications. However, as CT contrast agents, lanthanide-based nanomaterials require a relatively high unit dose to enhance contrast, inevitably increasing the cost and toxicity risks. We tabulated the properties and characteristics of the representative CT contrast agents for clarity of presentation (**Table 2**).

Table 2. List of contrast agents for CT imaging in biomedicine

Element and atomic number	K-edge energy [keV]	X-ray mass attenuation coefficient at 100 keV [cm ² g ⁻¹]	Representative contrast agents	Advantages	Disadvantages	Therapeutic application	References
I (53)	33.2	1.94	Iopromide, Iodixanol, Iohexol, Meglumine diatrizoate	Low-cost, large-scale production, wide application in clinical practice	Low contrast, short retention time <i>in vivo</i> , allergic reaction, nephrotoxicity	NA	[8]
Lanthanide elements							
Ce (58)	40.4	2.45	CeO ₂ NPs	High colloidal stabilities, rich in resources	Low yield, short circulation times, nephrotoxicity	PTT, PDT, RT, starvation therapy, gas therapy	[71]
Eu (63)	48.5	3.04	Eu ₂ O ₃ NPs				[70]
Gd (64)	50.2	3.11	Gd ₂ O ₃ NPs				[68]
Ho (67)	55.6	3.49	NaHoF ₄ NPs				[74]
Er (68)	57.5	3.63	NaErF ₄ NPs				[75]
Yb (70)	61.3	3.88	NaYbF ₄ NPs				[77]
Lu (71)	63.3	4.03	NaYF ₄ :Nd ³⁺ @NaLuF ₄				[83]
Transition metal elements							
Hf (72)	65.3	4.15	HfO ₂ NPs	Physiological inertness, easy of functionalization	Complex syntheses, relatively high-cost	PTT, RT, chemotherapy	[89]
Ta (73)	67.4	4.30	TaOx NPs				[92]
W (74)	69.5	4.44	RbxWO ₃ NRs				[97]
Re (75)	71.7	4.59	ReS ₂ NSs				[99]
Ir (77)	76.1	4.86	Ir-Ag-IrO ₂ NPs				[101]
Pt (78)	78.4	4.99	Pt Spirals				[103]
Gold element							
Au (79)	80.7	5.16	AuNSp, AuNSs, AuNRs, AuNCs, AuNShs	Mature preparation methods, easy surface modification, high biocompatibility	High-cost, hepatotoxicity	PTT, PDT, RT, SDT, GI, immunotherapy, chemotherapy	[14-27]
Bismuth element							
Bi (83)	90.5	5.74	Bi ₂ S ₃ NPs, Bi ₂ Se ₃ NPs, Bi ₂ O ₃ NPs, Cu ₃ BiS ₅ NPs	High X-ray attenuation capability, relatively low toxicity, low-cost	Poor solubility, limited contrast effect at low X-ray tube voltages (< 80 keV)	PTT, PDT, RT, SDT, gas therapy, chemotherapy	[56-62, 64-65]

PPT: photothermal therapy; PDT: photodynamic therapy; RT: radiotherapy; SDT: sonodynamic therapy; GI: gene therapy; MWTT: microwave thermal therapy.

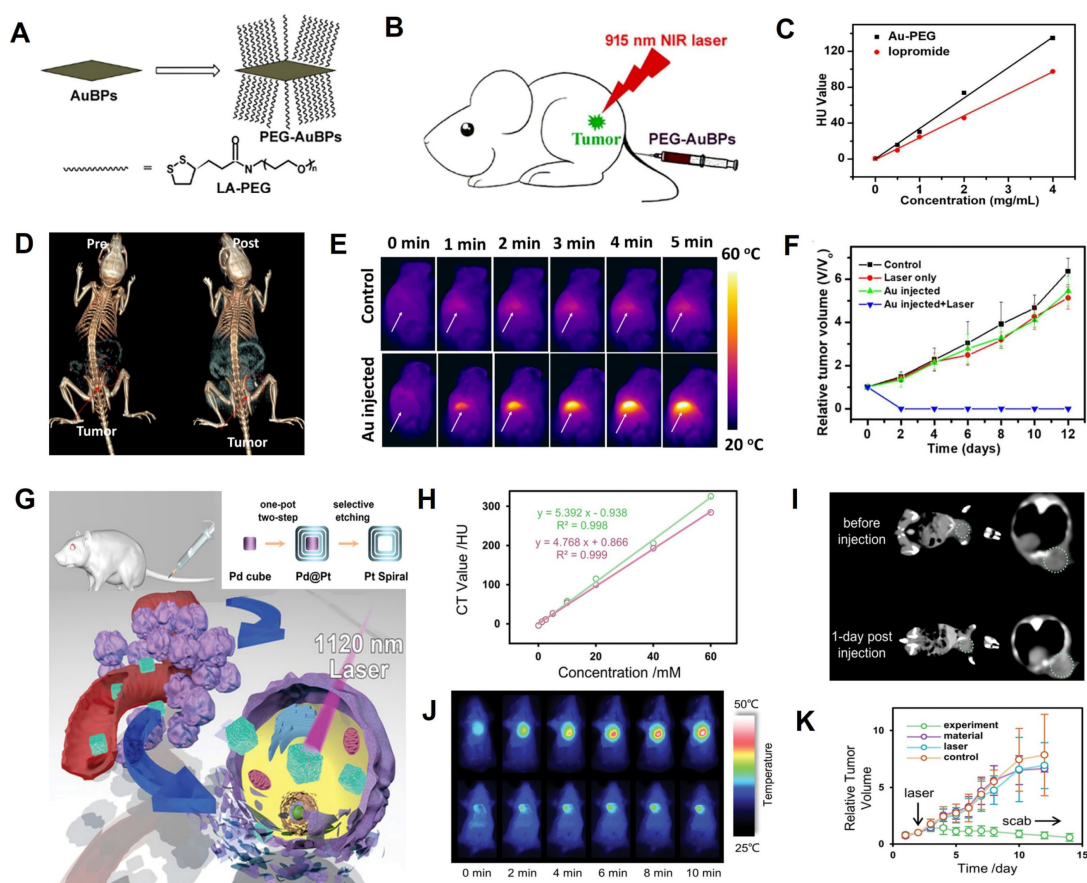


Figure 6. CT image-guided PTT. (A) Synthesis and modification of PEG-AuBPs. (B) Schematic illustration of AuBPs for CT image-guided PTT. (C) Concentration-dependent change in CT values of PEG-AuBPs and iopromide. (D) CT images of 4T1 tumor-bearing mice at pre- and post-intravenous injection. (E) Changes in thermal images of 4T1 tumor-bearing mice. (F) Relative tumor volume after various treatments. (G) Schematic diagram of the synthesis and treatment of Pt Spirals. (H) CT values of Pt Spirals and Omnipaque at different concentrations. (I) CT images of tumor-bearing mice at pre- and post-intravenous injection of Pt Spirals. (J) Thermal images of tumor-bearing mice. (K) Relative tumor volume in different groups. (A-F) Adapted with permission from [119]. Copyright 2019 Elsevier. (G-K) Adapted with permission from [103]. Copyright 2019 Wiley-VCH.

CT image-guided therapy

Current non-surgical therapeutic options for cancer mainly include chemotherapy and radiotherapy (RT), causing significant collateral damage [108]. Although chemotherapeutic drugs kill cancer cells, they may cause severe harm to normal cells due to their non-selective effects. Radiation employed in RT may impact neighboring organs due to oxygen-free radicals produced during the radiation [109, 110]. New nanoagents with diagnosis and treatment functions have been developed benefiting from molecular imaging and nanotechnology. The nanoagents are utilized in photothermal therapy (PTT), photodynamic therapy (PDT), gene therapy (GT), immunotherapy, gas therapy, sonodynamic therapy (SDT), starvation therapy *etc.* These emerging treatment modalities are expected to mitigate the side effects of traditional treatments and improve treatment efficiency. Here, we will focus on CT image-guided cancer treatment.

Photothermal therapy

PTT is a promising cancer therapy method that

uses NIR light to excite photothermal agents (PTAs) delivered to the tumor region [111, 112]. PTAs absorb and convert light energy to heat, resulting in local hyperthermia to kill cancer cells [113-116]. AuNPs, including hollow spherical structures [117], nanorods [118], bipyramids [119], and nanostars [120], are excellent CT contrast agents and PTAs due to their high X-ray attenuation coefficient and superior photothermal conversion efficiency (PCE) [121]. Zhang *et al.* designed PEG-functionalized mono-disperse gold bipyramids (AuBPs) with controlled aspect ratio and tunable surface plasmon resonance (SPR) property, which can tune the absorption wavelength to NIR region and significantly enhance the light absorption cross-section for CT image-guided PTT (Figure 6A-B) [119]. The CT value increased linearly with the increasing concentration of PEG-AuBPs and was higher than that of iopromide at the same concentration (Figure 6C). After intravenous administration of PEG-AuBPs to 4T1 tumor-bearing mice, the contrast at the tumor site increased significantly over time and reached a maximum at 24 h post-injection, indicating significant enrichment of PEG-AuBPs at the tumor site (Figure 6D). Given the

CT imaging result, PTT was carried out at 24 h post-injection and the temperature of the tumor site increased from 35 °C to 52 °C after 5 min of 915 nm laser irradiation (**Figure 6E**), generating hyperthermia to kill tumor cells effectively (**Figure 6F**).

However, limited by low maximum permissible exposure (MPE, 0.33 W cm⁻²) of the first near-infrared bio-window (NIR-I, 700-1000 nm) for skin [122], the efficacy of PTT was poor [123]. PTT triggered by the second near-infrared bio-window (NIR-II, 1000-1350 nm), generated widespread concern due to its deeper penetration depth of biological tissues, lower photon scattering, and higher MPE (1.0 W cm⁻²) [124]. Wang *et al.* synthesized hollow Pt nanoframes ("Pt spirals") by a simple selective etching strategy, which exhibited high PCE (52.5%) and strong molar extinction coefficients (MEC, 228.7 m² mol⁻¹) in NIR-II window (**Figure 6G**) [103]. Pt nanostructures also had a high K-edge value (78.4 keV), endowing them with great potential for CT image-guided PTT. Also, Pt spirals exhibited higher contrast efficacy than the iodine-containing agent (Omnipaque) at equivalent concentrations (**Figure 6H**); 24 h after intravenous injection of Pt spirals, the CT value of the tumor site increased from 37.5 HU to 58.2 HU (**Figure 6I**), indicating the maximum enrichment. Therefore, 24 h was selected as the starting time point of treatment. Based on the location information provided by CT imaging, the tumor region of the mouse was irradiated with an 1120 nm laser at 24 h post-injection. The temperature in the tumor region reached an average value of 49.9 °C in the experimental group after 10 min of irradiation, which was significantly higher than (41.9 °C) in the control group (**Figure 6J**), and the tumor completely ablated at 10 days post-treatment (**Figure 6K**). These results illustrated that CT image-guided PTT might hold great potential for future biomedical applications.

Photodynamic therapy

PDT takes advantage of the cytotoxicity of ROS generated by the reaction of photosensitizers (PSs) and oxygen (O₂) in light irradiation to kill tumor cells [125]. However, hypoxic TME and low light penetration depth limit the application of PDT in biomedicine. Therefore, multifunctional nanoagents with CT imaging, NIR absorption, and catalytic O₂ generation capabilities are expected to address the PDT disadvantage.

Hypoxia in the tumor may be alleviated by catalyzing the production of O₂ from H₂O₂, which is overexpressed in cancer cells [126, 127]. Zhao *et al.* designed c(RGDyK)-targeting and catalase-modified Ce6-loaded AuNSs (ASCE-R) for CT image-guided PDT (**Figure 7A**) [128]. Because of the high expression

of α_vβ₃ receptor in HeLa cells, the CT values of HeLa cells incubated with ASCE-R exhibited higher CT values (94.85 HU) compared with MCF-7 cells (low expression of the α_vβ₃ receptor) incubated with ASCE-R (74.45 HU), indicating that ASCE-R presented outstanding tumor-targeting, CT imaging capability (**Figure 7B**). Meanwhile, the ASCE-R showed an excellent O₂ production rate (23 mg/mL, **Figure 7C**), confirming that catalase in the probe could catalyze H₂O₂ to O₂. The CT signal at the tumor site was observed 24 h after injection of the ASCE-R probe and peaked at 72 h, demonstrating the excellent intratumoral retention capability of ASCE-R (**Figure 7D**). At this time point, the tumor site was irradiated with the NIR laser at 660 nm, and the tumor perished 26 d post-irradiation, demonstrating the excellent CT image-guided PDT effect achieved by ASCE-R as a versatile nanoagent (**Figure 7E**).

Furthermore, light in the NIR-II window affords greater penetration depth and lower photo-toxicity to normal tissues than light in the visible and NIR-I windows [129]. Xu *et al.* fabricated isotropically plasmonic bimetal Pt-tipped AuNRs with zeolitic imidazolate framework-8 (Pt-tipped Au@ZIF-8) for CT image-guided PDT, which presented efficient plasmon-induced electron-hole spatial separation with 1064 nm laser irradiation and excellent CT imaging performance (**Figure 7F-G**) [130]. Meanwhile, nano-Pt with catalase-like activity could catalyze H₂O₂ overexpressed in TME to generate O₂ and relieve tumor hypoxia (**Figure 7H**). After injection, a significantly enhanced CT signal was observed at the tumor site. Thus, CT imaging could be used to determine the region of NIR-II laser irradiation and monitor the treatment effect (**Figure 7I**). Tumor tissue showed significantly weak hypoxia green fluorescence 24 h after injection of Pt-tipped Au@ZIF-8 by immunofluorescence staining assay with hypoxia-inducible factor (HIF)-1α (**Figure 7J**), demonstrating that Pt-tipped Au@ZIF-8 could efficiently alleviate tumor hypoxia. Also, tumor volume was significantly reduced in the Pt-tipped Au@ZIF-8 group after 12 days of treatment with 1064 nm laser irradiation guided by CT imaging (**Figure 7K**).

Chemotherapy

Conventional chemotherapy drugs have several drawbacks, including low selectivity, high toxicity, and insufficient efficacy [131]. The CT-guided NP delivery systems can overcome the limitations of traditional chemotherapy [132] by targeting the release of chemotherapy drugs to the tumor region, and have several advantages, including (1) controlled release in a specific site triggered by specific stimuli to

reduce damage to normal tissues [133], (2) targeted drug release to cancer cells to reduce side effects and increase the concentration of the drug in the target region [134], and (3) combined contrast agents to improve the efficiency of diagnosis and treatment [135].

Wang *et al.* prepared a drug delivery carrier (Au-BSA-DOX-FA NPs) consisting of BSA-modified Au NPs and anhydride-doxorubicin (cis-DOX) and FA for CT image-guided targeted chemotherapy in cancer tissues overexpressing folate receptor (FR) (Figure 8A) [136]. Quantification of DOX in different pH media indicated that the aconityl linker between DOX and Au-BSA NPs was readily broken and released about 90% DOX at pH 5.0 (Figure 8B), indicating excellent pH-responsive drug release capability of Au-BSA-DOX-FA NPs. After intravenous administration, the CT values of the tumor site in the Au-BSA-DOX-FA NP-targeted group were markedly higher than the non-targeted group at 30 min post-injection (Figure 8C), indicating that the TME-responsive drug delivery system could achieve targeted drug delivery. In addition, the tumor volume at 20 days after intravenous administration of Au-

BSA-DOX-FA was significantly reduced compared with the control group (0.25 *vs.* 0.88 cm³, Figure 8D).

Magnetic nanocomposites, such as Fe₃O₄ NPs, loaded with chemotherapy drugs can also be released into target tumor tissues *via* magnetic orientation and CT localization. Kitaev *et al.* fabricated a polyvinyl alcohol (PVA)-encapsulated DXL (docetaxel, a chemotherapeutic drug)-loaded dual (temperature and pH)-responsive magnetically directed plasmonic nanocomposite (Au/Fe₃O₄/PVA-10%DXL) for CT image-guided chemotherapy [137]. After 12 h of application of a 1 Tesla magnetic field to the tumor-bearing mouse, the Au/Fe₃O₄/PVA-10%DXL nanocomposite was navigated to the cancer site, as confirmed by CT scans (Figure 8E-F). At this time point, the high temperature produced by 808 nm NIR irradiation and acidic TME controlled DXL release. Thus, Au/Fe₃O₄/PVA-10% DXL exhibited efficient selective release (\approx [96 \pm 3]%) of DXL) and the tumor inhibition effect ([70 \pm 6.3]%) (Figure 8G-H).

Pt can be used as a CT contrast agent and, due to its inherent antitumor effect, can also be used for synthesizing chemotherapy drugs, such as Cisplatin and Carboplatin [138]. However, high concentrations

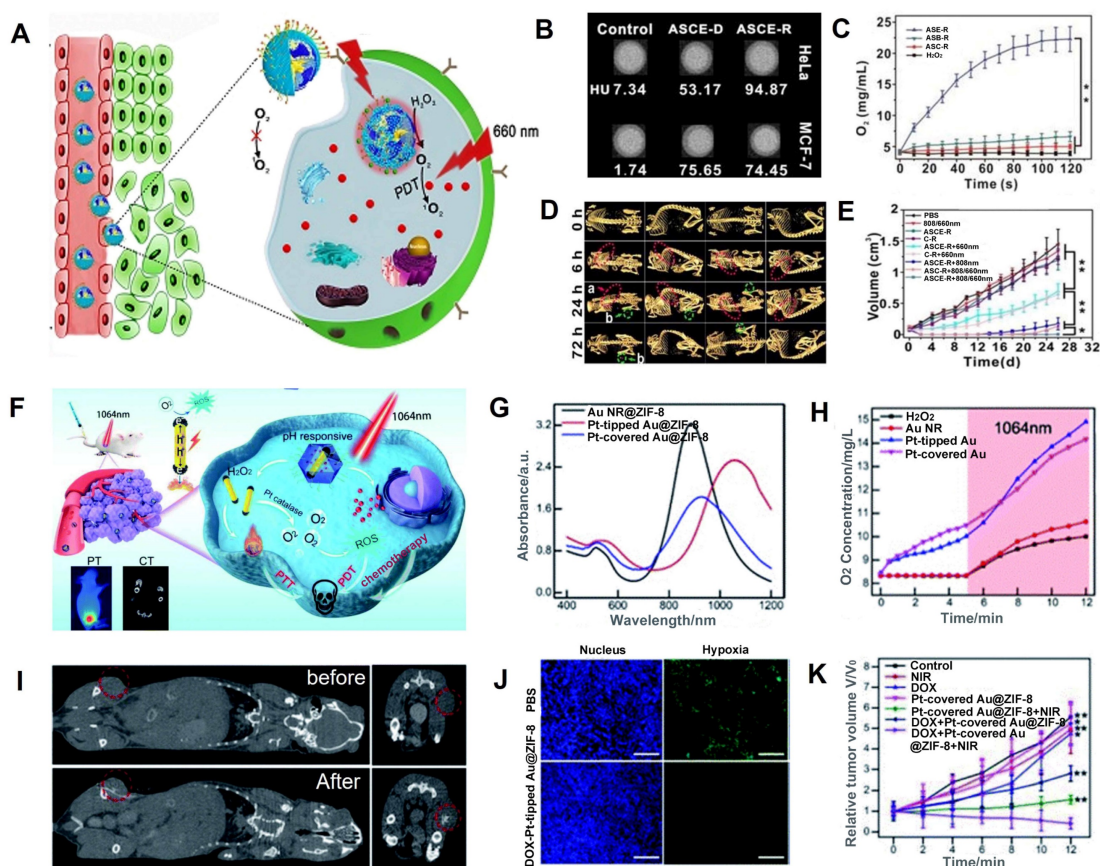


Figure 7. CT image-guided PDT. (A) Schematic illustration of CT image-guided PDT. (B) CT signal intensity of the nanomaterial. (C) O₂ production curve of different probes. (D) *In vivo* CT imaging. (E) Tumor volume after different treatments. (F) Schematic illustration of the CT image-guided PDT. (G) UV-vis-NIR absorption spectra of Pt-tipped Au@ZIF-8. (H) O₂ generation under 1064 nm laser irradiation. (I) CT images of tumor-bearing mice before and after intratumoral injection. (J) HIF-1 α staining of 4T1 tumor in different treatment groups. (K) Relative tumor volume after different treatments. (A-E) Adapted with permission from [128], Copyright 2019 Ivyspring International Publisher. (F-K) Adapted with permission from [130], Copyright 2021 The Royal Society of Chemistry.

of Pt must be maintained to obtain satisfactory CT imaging results, raising the possibility of serious side effects [139]. Recently, Huang *et al.* synthesized reductant-sensitive bio-Pt-I NPs consisting of iodine-conjugated Pt (IV) compounds and biotin as a theranostic nanomedicine for CT image-guided treatment (**Figure 8I**) [140]. The bio-Pt-I NPs with high Pt (25.36%) and I (32.99%) contents could be used for CT imaging and real-time dynamic distribution monitoring of nanomedicines. CT signal intensity increased as a function of bio-Pt-I NP concentration (**Figure 8J**). After intravenous administration of bio-Pt-I NPs, the CT signal at the tumor site was significantly enhanced at 6 h, peaked at 12 h, and remained until 24 h post-injection, enabling visualization of the enrichment of bio-Pt-I NPs in tumors (**Figure 8K**). In addition, the bio-Pt-I exhibited a stronger CT imaging signal (1680 HU) than bio-Pt-Cl

(1126 HU) at the same concentration due to the iodine element (**Figure 8L**). Furthermore, Pt (IV) in the bio-Pt-I NPs could be reduced to Pt (II) by GSH overexpressed in tumor cells, leading to a controlled release of active Pt (II) segments to improve antitumor outcomes (**Figure 8M**).

Radiotherapy

Radiotherapy is one of the most effective treatment options for cancer, but radioresistance is a significant challenge [141-143]. Therefore, it is imperative to develop nanoagents with radiosensitization to improve the RT effect.

The surface of AuNPs produces secondary electrons or Auger electrons *via* the photoelectric effect when it absorbs low and medium-energy X-ray (<250 keV), improving the local RT effect and reducing the damage to normal tissues due to the

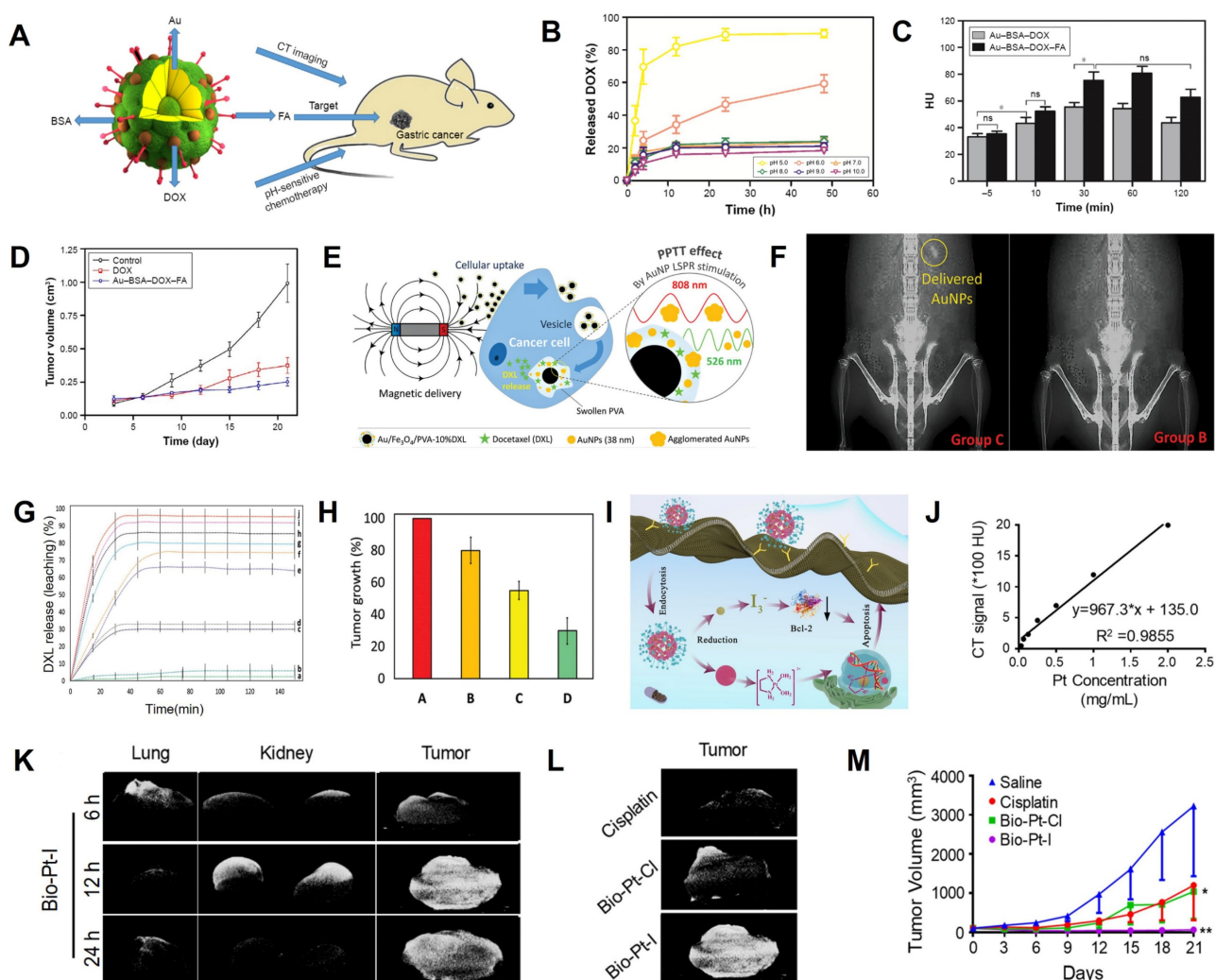


Figure 8. CT image-guided chemotherapy. **(A)** Schematic illustration of Au-BSA-DOX-FA nanocomposite for CT image-guided chemotherapy. **(B)** Release of DOX at different pH values. **(C)** CT values of gastric cancer tissues. **(D)** Tumor volumes. **(E)** Schematics of magnetically-delivered and released drugs, and **(F)** Corresponding CT images. **(G)** Release profiles of DXL from Au/Fe₃O₄/PVA-10%DXL. **(H)** Tumor growth at 14 days post-treatment. **(I)** Antitumor mechanism of I-Pt-Bio NPs. **(J)** CT values at various concentration of Bio-Pt-I NPs. **(K)** CT images of major organs of mice at different times. **(L)** CT images of mice after treatment with Bio-Pt-Cl and Bio-Pt-I for 12 h. **(M)** Tumor growth curves after different treatments. **(A-D)** Adapted with permission from [136], Copyright 2017 Dove Press Ltd. **(E-H)** Adapted with permission from [137], Copyright 2020 Wiley-VCH. **(I-M)** Adapted with permission from [140], Copyright 2022 American Chemical Society.

short range of the secondary electrons (**Figure 9A**) [144-146]. Chang *et al.* synthesized PEGylated ~13 nm AuNPs for CT image-guided RT because of their superior CT contrast and radio-sensitization properties [15]. The CT value of PEGylated AuNPs was 1.2 times that of iohexol (**Figure 9B**) and their sensitization enhancement ratio (SER) was twice that of CMNa (a clinical radiosensitizer) (**Figure 9C**). Also, the CT signal at tumor region was 1.8-fold higher than iohexol 90 min after intravenous administration of the PEGylated AuNPs (**Figure 9D**). When the tumor was exposed to 6 Gy of X-ray irradiation at 90 min post-injection, the growth of the tumor was dramatically inhibited with a 61.26% increase in radio-sensitization compared to RT alone (**Figure 9E**).

Cancer cells are three times more radioresistant in hypoxia than in aerobic conditions, which has been attributed to the mechanism by which DNA damage by ionizing radiation can be easily repaired in the absence of O₂ [147]. MnO₂ with a catalase-mimic catalytic activity can catalyze overexpressed H₂O₂ in tumors to generate O₂, thus relieving tumor hypoxia [148-150]. Shi *et al.* synthesized intelligent Au/MnO₂-coloaded poly(N-vinylcaprolactam) (PVCL-Au-

MnO₂) nanogels (NGs) for CT image-guided RT; PVCL-Au-MnO₂ NGs with a catalase-mimic catalytic activity could convert H₂O₂ in tumors to generate O₂ to improve the radio-sensitization effect (**Figure 9F**) [151]. The CT value increased linearly as a function of the PVCL-Au-MnO₂ NG concentration. A significant CT signal enhancement at the tumor site (the CT value increased from 21.7 ± 1.6 HU to 436.3 ± 3.8 HU) was observed 24 h after intravenous injection (**Figure 9G**), indicating that PVCL-Au-MnO₂ NGs enabled the efficient accumulation of O₂ in tumor regions. Besides, immunofluorescence images and intensity analysis showed that the percentage of hypoxic tumor areas decreased from 67.6% at pre-injection to 25.3% at 24 h post-injection (**Figure 9H**), confirming that the PVCL-Au-MnO₂ NGs could relieve tumor hypoxia. Therefore, CT imaging results were used to determine the location and start time of X-ray irradiation. When the tumor was exposed to 4 Gy of X-ray irradiation at 24 h post-injection, the growth of the tumor was significantly inhibited with an SER of ~1.49 at 20 days post-irradiation (**Figure 9I**), indicating that the PVCL-Au-MnO₂ NGs possessed an excellent CT-guided radio-sensitization effect.

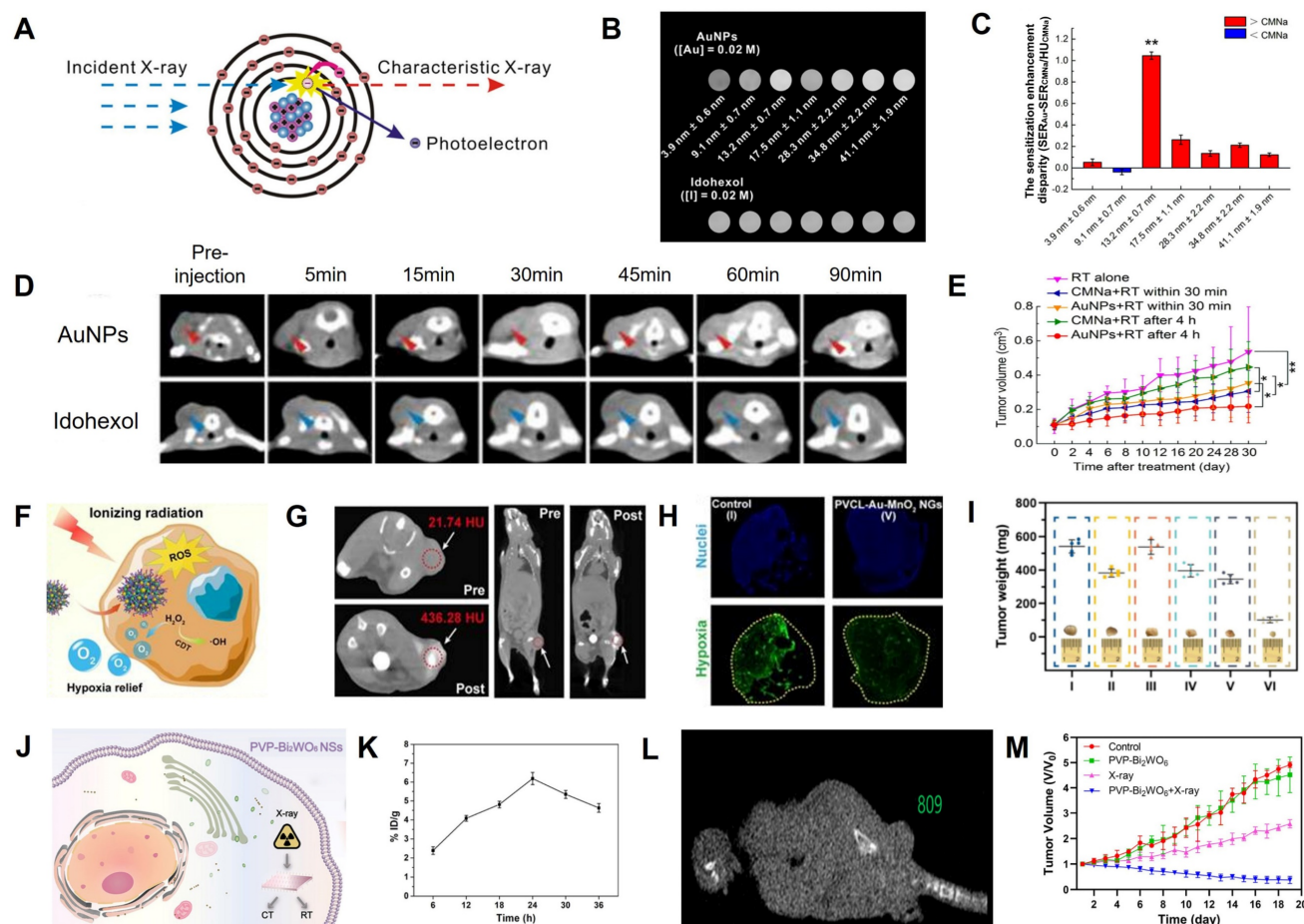


Figure 9. CT image-guided radiotherapy. **(A)** Proposed mechanism of the photoelectric effect. **(B)** CT signal intensities of different sizes of AuNPs and Iohexol at the same concentration. **(C)** Sensitization enhancement disparity between AuNPs and CMNas for various particle sizes under 6 Gy radiation. **(D)** *In vivo* CT images after intravenous administration of AuNPs and Iohexol. **(E)** Tumor growth inhibition curves after various treatments. **(F)** Schematic diagram of PVCL-Au-MnO₂ NGs for radio-sensitization. **(G)** *In vivo* CT images of mice before and at 24

h post intravenous injection. (H) Hypoxia-positive immunofluorescence images. (I) Tumor weight after different treatments. (J) Schematic diagram of PVP-Bi₂WO₆ NSs for CT image-guided RT. (K) Aggregate amount and (L) CT values at 24 h post-intravenous injection of PVP-Bi₂WO₆ NS. (M) Tumor volume after various treatments. (A-E) Adapted with permission from [15], Copyright 2016 American Chemical Society. (F-I) Adapted with permission from [151], Copyright 2022 Ivspring International Publisher. (J-M) Adapted with permission from [153], Copyright 2022 American Chemical Society.

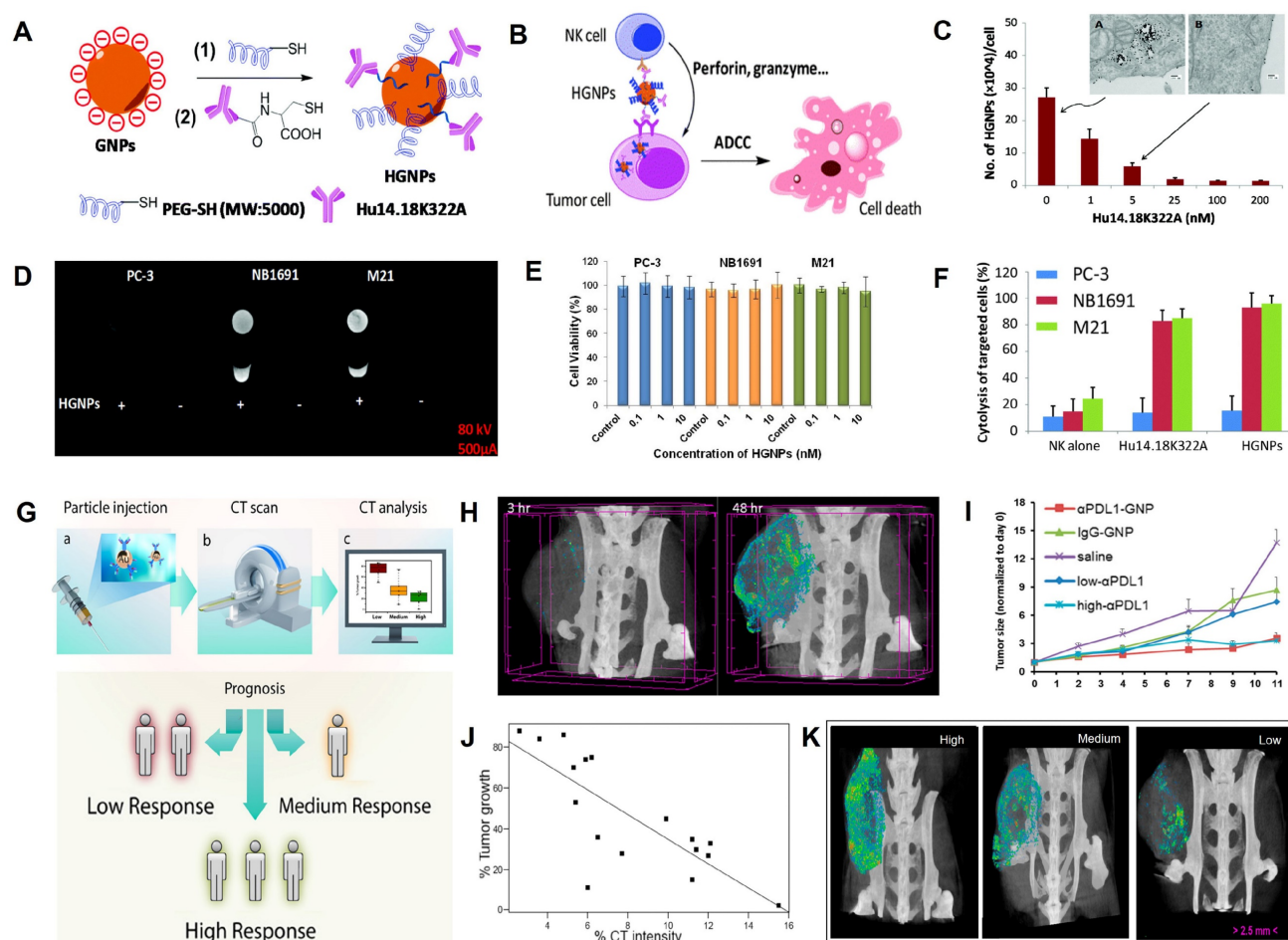


Figure 10. CT image-guided immunotherapy. (A) Synthesis of HGPNs. (B) Schematic illustration of HGNP-mediated immunotherapy. (C) Internalization of HGPNs in M21 cells. (D) CT images of PC-3, NB1691, and M21 cell pellets. (E) Cytotoxicity of HGPNs to the PC-3, NB1691, and M21 without NK cells. (F) Cytotoxicity of HGPNs to the PC-3, NB1691, and M21 with NK cells. (G) Schematic illustration of immune reactivity prediction via CT imaging. (H) CT signals in tumor sites of mice at different times. (I) Tumor growth rate in different treatment groups. (J) Correlation between CT signal intensity and therapeutic outcomes. (K) CT image-guided stratification. (A-F) Adapted with permission from [157], Copyright 2016 The Royal Society of Chemistry. (G-K) Adapted with permission from [163], Copyright 2017 American Chemical Society.

The radiosensitization effect of BiNPs is approximately 1.25-fold higher than AuNPs [152]. Li *et al.* prepared PVP-modified Bi₂WO₆ NSs by the hydrothermal synthesis method for CT image-guided RT (Figure 9J) [153]. The CT values and the accumulation rate at the tumor site was 809 HU and 6.19%, respectively, 24 h after intravenous injection of PVP-Bi₂WO₆ NSs (Figure 9K-L); therefore, this time point was identified as the point of initiation of treatment. The SER was calculated to be ~2.65 after 18 days of RT, and the tumors in mice were completely inhibited (Figure 9M).

Immunotherapy

Immunotherapy often uses a combination of antigens and antibodies to help the host recognize the tumor and stimulate the immune system to activate immune cells to kill the tumor [154, 155]. However, free antigens are easily inactivated by enzymes in

blood circulation [155, 156]. Therefore, nanomaterials with imaging capabilities are used as carriers for the targeted transport of these antigens, enabling antigen protection and real-time efficacy monitoring. Yan *et al.* designed a nanotracer (named HGPNs) consisting of AuNPs and hu14.18K322A (a tumor-targeting anti-GD2 antibody) for attacking and killing specifically cancer cells through antibody-dependent natural killer (NK) cell-mediated cytotoxicity (ADCC) and realizing CT image-guided immunotherapy (Figure 10A-B) [157]. After incubation with HGPNs for 12 h, the CT signal intensity of neuroblastoma NB1691 and melanoma M21 cells (GD2-positive cells) was 5.27- and 7.66-fold, respectively, of that before incubation with HGPNs. While GD2-negative PC-3 cells remained essentially unchanged before and after incubation (Figure 10C-D), these results demonstrated that HGPNs had excellent cell-targeting

capabilities. When combined with NK cells, HG NPs induced significant ADCC and killed almost 100% of the GD2-positive target, while there was no appreciable therapeutic effect on GD2-negative PC-3 cells, indicating that HG NPs had excellent targeted immunotherapy capabilities (**Figure 10E-F**).

Only a small number of patients can benefit from immunotherapy due to the lack of effective stratification of patients [158]. Immune checkpoints overexpressed on tumor cells, such as programmed death ligand 1 (PDL1), inhibit the antitumor immunoreaction [159-162]. However, immune checkpoint blockade (ICB) therapy has a limited success rate of no more than 30%; therefore, early identification of subjects who benefit from ICB therapy through CT imaging techniques is crucial to cancer treatment decisions. Popovtzer *et al.* designed programmed death ligand 1 antibody (α PDL1)-modified AuNP nanoagents (α PDL1-AuNPs) with CT imaging and therapy functions for achieving the integration of hierarchical diagnosis and treatment (**Figure 10G**) [163]. The PDL1 expression dramatically reduced from 86.6% to 23.9% when MC38 colon carcinoma cells were incubated with α PDL1-AuNPs, demonstrating that the immune checkpoint ligand on the cell surface could bind with α PDL1-AuNPs and facilitate T cell activation. Moreover, α PDL1-AuNPs, as a CT contrast agent, were able to track the *in vivo* distribution and evaluate the treatment effect. After α PDL1-AuNPs were intravenously injected into MC38 colon carcinoma cell-bearing mice, the maximum accumulation of the nanoprobe occurred at 48 h post-injection (**Figure 10H**), and the tumor growth rate was significantly inhibited (**Figure 10I**). Subsequently, the early prediction of therapeutic response was performed by intravenously injecting α PDL1-AuNPs into 20 tumor-bearing mice, and the tumor size was measured at 48 h post-injection through CT scan and 8 days post-injection *via* calipers. The results showed that the quantitative CT signal at 48 h post-injection and tumor size at 8 days post-injection were linearly correlated ($R^2 = 0.6162$, **Figure 10J**), demonstrating that the combination of α PDL1-AuNPs and CT imaging could predict therapeutic response as early as 48 h after treatment (**Figure 10K**).

Starvation therapy

As an emergent cancer treatment strategy, starvation therapy could effectively inhibit tumor growth by cutting off the nutrient (glucose) supply of the tumor [164-166]. Glucose oxidase (GOD) is a type of oxidoreductase that converts glucose, O_2 , and water into gluconic acid and H_2O_2 [167]. However, this reaction highly depends on the on-site O_2 content, and alleviating hypoxia at the tumor site is a prerequisite

for starvation therapy in treating tumors [168].

Zhang *et al.* developed a GOD-loaded catalase (CAT)-like biocatalyst (PEGylated UCNPs@mSiO₂@CeO₂-GOD, USC GP) with strong X-ray attenuation capability and O_2 self-generation function for CT image-guided synergistic starvation therapy and PDT (**Figure 11A**) [169]. The CT value gradually increased with the increasing concentration of USC GP and was 3-fold higher than ioversol at the same concentration, indicating the superior CT imaging capability of USC GP (**Figure 11B**). After intravenous injection of USC GP, the CT values at the tumor site increased gradually from 18.8 HU (pre-injection) to 48.3 HU (12 h post-injection), indicating that USC GP could effectively accumulate at the tumor site (**Figure 11C-D**). As shown in **Figure 11E**, when USC GP was internalized into tumor cells, intratumoral overexpressed H_2O_2 was decomposed into O_2 by catalysis of USC GP with CAT-like activity. Catalyzed by GOD, the resulting O_2 reacted with endogenous glucose to generate H_2O_2 , and glucose was consumed for starvation therapy. In addition, highly toxic $\bullet OH$ was produced under NIR laser illumination due to the involvement of CeO₂ with peroxidase (POD)-like activity and H_2O_2 , further killing cancer cells through PDT. After intravenous administration, the tumor was effectively inhibited at day 14 post-treatment (**Figure 11F**), indicating USC GP is a promising theranostic agent for CT image-guided synergistic therapy.

Ning *et al.* developed an adenovirus-mimicking nanomachine (AMN) consisting of AuNRs, GOD, BSA-MnO₂, and RGD peptide for image-guided synergistic starvation therapy and PTT (**Figure 11G**) [170]. AMN possessed adenovirus-like function, excellent cancer cell uptake, and tumor targeting capability. AMN also facilitated glucose oxidase-triggered glucose oxidation *via in situ* oxygenation (**Figure 11H**) and photothermal effect (**Figure 11I**), which significantly inhibited the expression of heat shock proteins (HSPs) and, in turn, increased photothermal efficacy, leading to synergistic antitumor effects. After intravenous administration, the CT signal at the tumor site was detected at 4 h post-injection and reached a plateau at 12 h post-injection, indicating it to be the optimal timing (**Figure 11J**). Thus, the superior CT imaging capabilities of AMN enabled differentiation between tumors and normal tissues. Furthermore, AMN could selectively target the tumor region and effectively eliminate the tumor after intravenous administration (**Figure 11K**), demonstrating that the virus-like nanotheranostic platform could potentially promote the development of complementary modalities for cancer therapy.

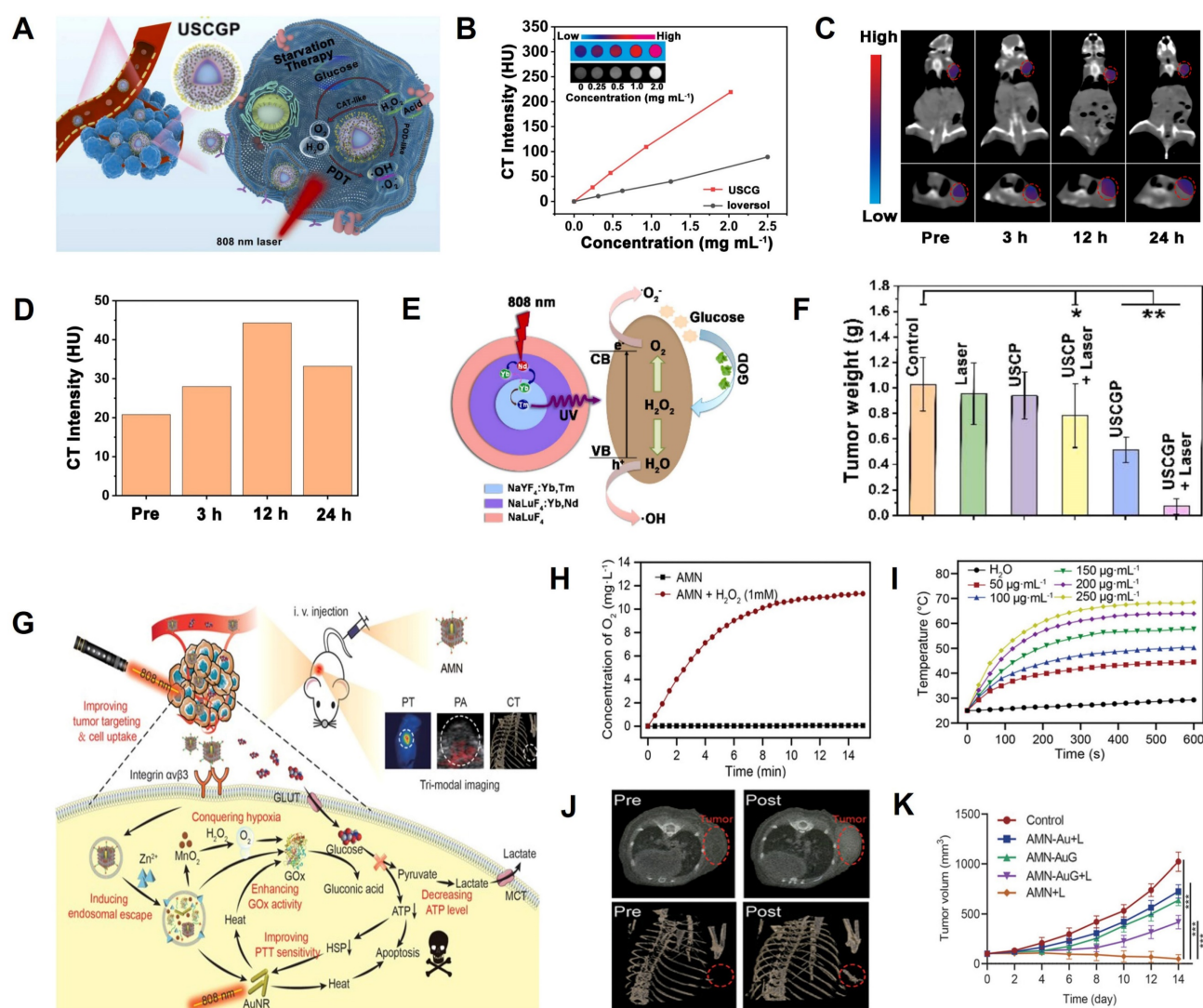


Figure 11. CT image-guided starvation therapy. (A) Schematic illustration of USCGP biocatalyst for starvation therapy. (B) Concentration-dependent CT signals of ioversol and USC. (C) CT contrast of 4T1 tumor-bearing mouse. (D) CT signal intensities of tumor area at different time points. (E) Photocatalysis mechanism of USC. (F) Tumor weight after 14 days of treatment. (G) Mechanism of AMN for glucose metabolism. (H) Time-dependent AMN-catalyzed O₂ generation. (I) Photothermal effect of AMN. (J) CT images of tumor-bearing mice pre- and post-injection of AMN. (K) Tumor volume changes. (A-F) Adapted with permission from [169], Copyright 2022 Elsevier. (G-K) Adapted with permission from [170], Copyright 2021 Wiley-VCH.

Gas therapy

As a “green” cancer therapy approach, gas therapy (e.g., NO, H₂S, CO, H₂, SO₂, and CO₂) has attracted increasing attention due to its low toxicity, minimal side effects, and low drug resistance [171]. Nitric oxide (NO) is a vasodilatation factor that can relieve the hypoxia status of tumor cells and enhance their sensitivity to RT [172]. The high concentration of NO can also induce apoptosis of cancer cells by producing oxidative and nitrative stress, inhibiting DNA repair and cellular respiration, and enhancing inflammatory reactions [173]. Liu *et al.* developed a Cu²⁺-initiated NO-releasing nanoagents (UMNOCC-PEG) consisting of dendritic porous SiO₂, UCNPs, SNO, Ce6, and CuO₂ for CT image-guided synergistic gas, chemodynamic, and photodynamic therapy (Figure 12A) [174]. The CT value increased linearly

with increasing concentration of UMNOCC-PEG (Figure 12B). After intratumoral injection, the tumor site showed a significantly enhanced CT signal (360.6 HU) compared with pre-injection (20.3 HU, Figure 12C), indicating that UMNOCC-PEG possessed outstanding CT imaging capability. After intravenous administration, the signal intensity at the tumor region at 12 h post-injection was approximately 4-fold higher than pre-injection, demonstrating the superior tumor enrichment capability of UMNOCC-PEG. Meanwhile, the acidic TME accelerated the decomposition of CuO₂ and synchronously induced the Fenton-like catalytic reaction of Cu²⁺ and H₂O₂ to form highly toxic •OH. UMNOCC-PEG also alleviated tumor hypoxia and antioxidant capability through NO production and glutathione consumption and enhanced the efficiency of PDT and chemo-

dynamic therapy (CDT). Furthermore, NO and ROS could produce reactive nitrogen species (RNS) to destroy DNA and facilitate the therapeutic effect (Figure 12D-E). Therefore, the CT image-guided gas therapy-based synergistic therapy showed significant tumor inhibition efficiency (Figure 12F).

In another example, Yang *et al.* fabricated X-ray-triggered NO-released multifunctional Bi-based nanotheranostic Bi-SNO NPs for CT image-guided combination therapy of RT, PTT, and gas therapy (Figure 12G) [175]. The CT values increased linearly with increasing Bi-SNO NPs concentration after intratumoral injection, and the CT signal at the tumor region was significantly enhanced (232.21 HU) compared to pre-injection (47.52 HU), indicating that Bi-SNO NPs were an excellent CT contrast agent (Figure 12H). Subsequently, CT image-guided X-ray irradiation could break down the S-N bond and induce *in situ* release of NO in specific tumor regions, triggering gas therapy and RT. PTT was also realized under 808 nm NIR laser irradiation. Thus, the combination of gas therapy, RT, and PTT caused

apoptosis and necrosis of tumor cells and resulted in tumor volume reduction (Figure 12I-J).

Sonodynamic therapy

Sonodynamic therapy (SDT), which consists of low-intensity ultrasound (US) combined with sonosensitizers, has emerged as a burgeoning cancer treatment method since its development in the late 1980s. SDT uses sonosensitizers to absorb the US energy, producing a cavitation effect to excite O₂ and generate ROS for killing tumor cells [176-181]. Zhang *et al.* developed a dual-targeted sonosensitizer (Au-TiO₂-A-TPP) that was assembled by TiO₂ NSs and Au NCs modified with mitochondria-targeted triphenylphosphine (TPP) and cancer cell membrane-targeted AS1411 aptamer for CT image-guided SDT (Figure 13A) [182]. After intravenous injection of Au-TiO₂-A-TPP, the CT signal at the tumor region continuously increased and reached the maximum value at 24 h post-injection (Figure 13B), at which point the tumor region was irradiated with US. The Au-TiO₂ NSs enriched in the tumor absorbed the US

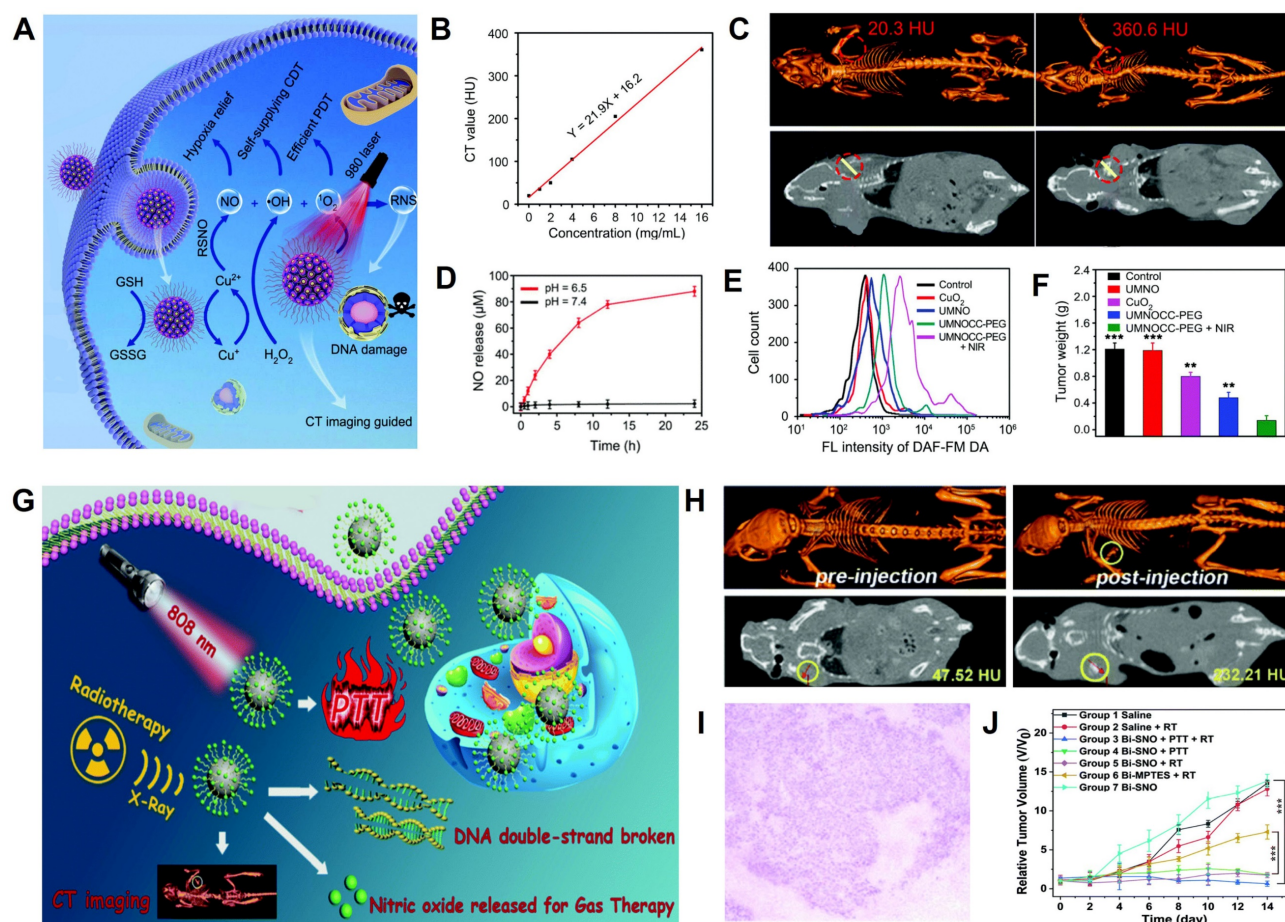


Figure 12. CT image-guided gas therapy. (A) Proposed mechanism of Cu²⁺-initiated multimodality therapy. (B) CT values as a function of concentration. (C) CT contrast of tumor-bearing mice at pre- and post-injection. (D) NO generation from UMNOCC-PEG under different pH values. (E) Intracellular NO by flow cytometry analysis. (F) Tumor weights of mice at 20-day post-treatment. (G) Schematic illustration of the Bi-SNO NPs for CT image-guided gas therapy. (H) CT contrast of tumor-bearing mice at pre- and post-injection. (I) H&E-stained image of tumor tissues. (J) Tumor volumes of mice in different treatment groups. (A-E) Adapted with permission from [174]. Copyright 2020 The Royal Society of Chemistry. (F-I) Adapted with permission from [175]. Copyright 2020 The Royal Society of Chemistry.

energy and facilitated the transfer of interfacial electrons under US irradiation, resulting in ROS production (Figure 13C). Consequently, the CT image-guided SDT resulted in efficient tumor growth inhibition and no recurrence (Figure 13D).

However, SDT depends on intratumor O₂ concentration, and the hypoxic TME compromises SDT efficiency. Therefore, increasing the O₂ content in the tumor region has become a major issue that must be addressed. Liu *et al.* synthesized targeting multifunctional hydrophilic nanomicelles AgBiS₂@DSPE-PEG₂₀₀₀-FA (ABS-FA), which had significant CT imaging capability and were used for the cascade-enhanced synergistic effect of SDT and PTT (Figure 13E) [183]. During the synergistic therapy, PTT heat could facilitate local blood circulation beneficial to alleviate the hypoxic TME. The CT values increased as a function of ABS-FA concentration, and the linear slope of ABS-FA was 43.21% higher than that of the traditional Bi₂S₃ NPs (Figure 13F) because the molar amount of metal per unit mass of AgBiS₂

was 1.35-fold higher than Bi₂S₃. Therefore, ABS-FA possessed a stronger X-ray attenuation to enhance the CT imaging capability. The reoxygenation of tumor cells was observed within 2 h after NIR laser irradiation because the photothermal effect could continuously alleviate hypoxia (Figure 13G). After intravenous injection of ABS-FA, CT signal intensity at the tumor site gradually increased over time and peaked at 6 h post-injection (Figure 13H), which was chosen as the starting time point for the ultrasound-photothermal synergistic therapy. The tumor volume was significantly inhibited 30 days after treatment (Figure 13I), suggesting that CT image-guided SDT-based therapy can open up new ways for clinical applications.

Gene therapy and microwave thermal therapy

Gene therapy (GT) can achieve long-term effects by introducing specific genes into target cells to repair defective genes or promote specific cellular functions [184, 185]. For example, FAM172A, as a functional

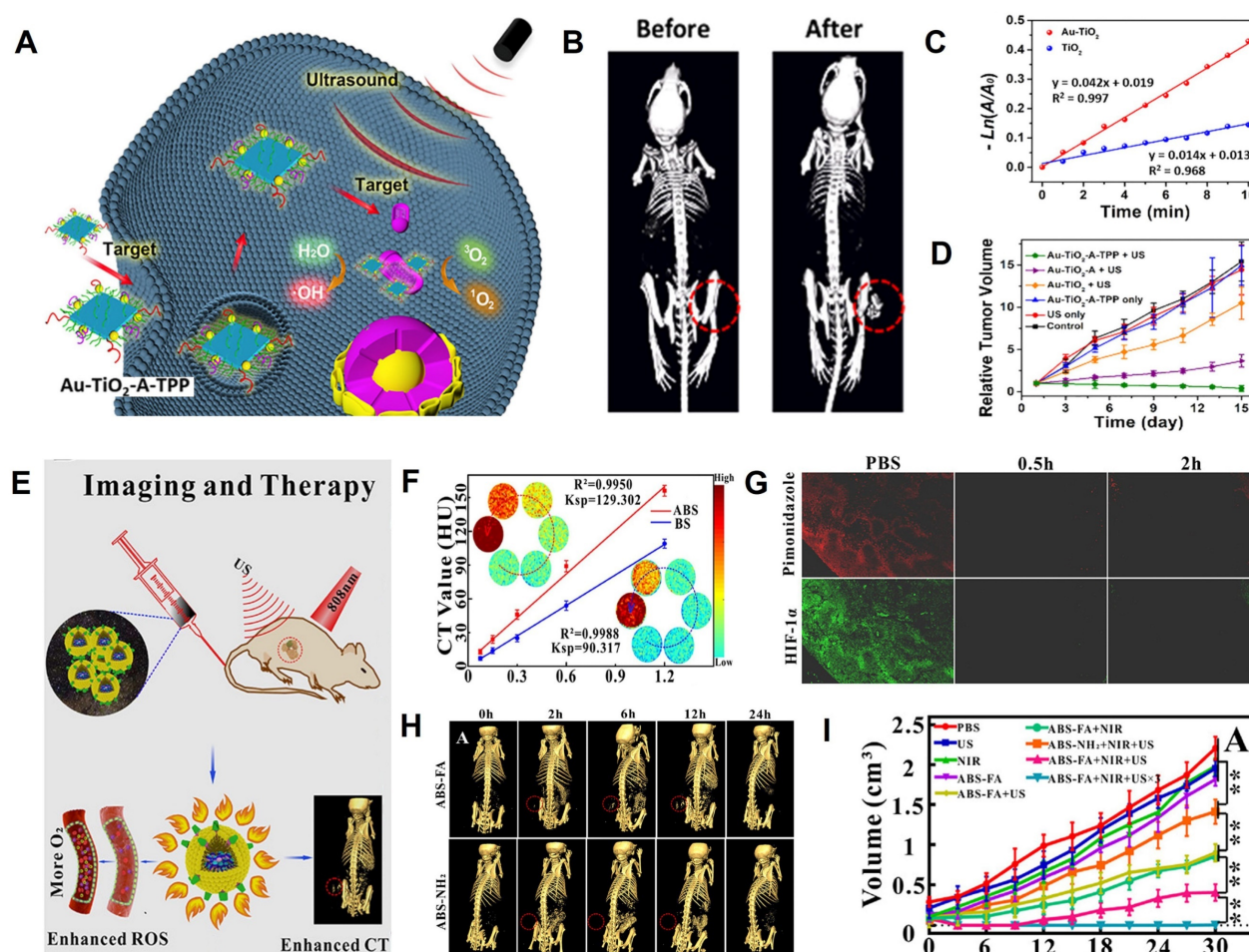


Figure 13. CT image-guided SDT. (A) Schematic illustration of dual-targeted Au-TiO₂-A-TPP for SDT. (B) CT images of tumor-bearing mice at pre- and post-intravenous Au-TiO₂-A-TPP injection. (C) O₂ generation under US irradiation. (D) Changes in relative tumor volumes. (E) Proposed principle of CT image-guided therapy. (F) CT values of ABS and BS at different concentrations. (G) Immunofluorescence staining of tumor site at 0.5 h and 2 h under ABS-FA plus NIR treatment. (H) Changes in CT contrast with time after injection of ABS-FA or ABS. (I) Tumor volumes in HeLa tumor-bearing mice. (A–D) Adapted with permission from [182], Copyright 2019 American Chemical Society. (E–I) Adapted with permission from [183], Copyright 2020 American Chemical Society.

gene, can inhibit the proliferation and accelerate apoptosis of colon cancer cells [186]. However, FAM172A is readily degraded by enzymes in the blood, so carrier protection is required to deliver FAM172A to the target region [187]. Therefore, Cui *et al.* designed the circular heptapeptide GX1-targeting multifunctional nanoagents (AuNR@PAMAM-GX1/FAM172A) consisting of dendrimer-modified AuNRs and FAM172A for CT image-guided GT/PTT of colon cancer cells (HCT-8 cells) (Figure 14A) [188]. After intravenous administration of AuNR@PAM-GX1/FAM172A to HCT-8 tumor-bearing nude mice, the CT signal at the tumor region gradually increased over time and peaked at 90 min post-injection, demonstrating the maximum enrichment of the AuNR@PAM-GX1/FAM172A in the tumor at that time point (Figure 14B). Based on CT imaging information, NIR irradiation at the tumor region was performed at 90 min post-injection to produce a photothermal effect, while the FAM172A was released for the combination of PTT and GT (Figure 14C-D).

Microwave (MW) thermal therapy (MWTT) is an emerging treatment method that promotes rapid heating and induces apoptosis in the tumor region through MW irradiation [189]. Meng *et al.* synthesized PEGylated IL-DOX-PCM-CuO@ZrO₂ multifunctional nanocomposites (IDPC@Zr-PEG) to upregulate tumor reoxygenation by utilizing CuO NPs to produce O₂ under MW irradiation in TME for improving the effect of combined cancer therapy of CT image-guided MWTT and chemotherapy (Figure 14E) [190]. The increase in CT values as a function of IDPC@Zr-PEG concentration due to the high atomic number of Zr demonstrated that IDPC@Zr-PEG possessed excellent CT imaging capabilities and can be used for real-time monitoring of tumor treatment. (Figure 14F). The MW irradiation of CuO enabled electron transfer and oxygen generation (Figure 14G) to alleviate hypoxia. CT values of the tumor region increased from 24 HU at pre-injection to 53 HU 24 h after intravenous injection of IDPC@Zr-PEG (Figure 14H). Based on the CT imaging information, the

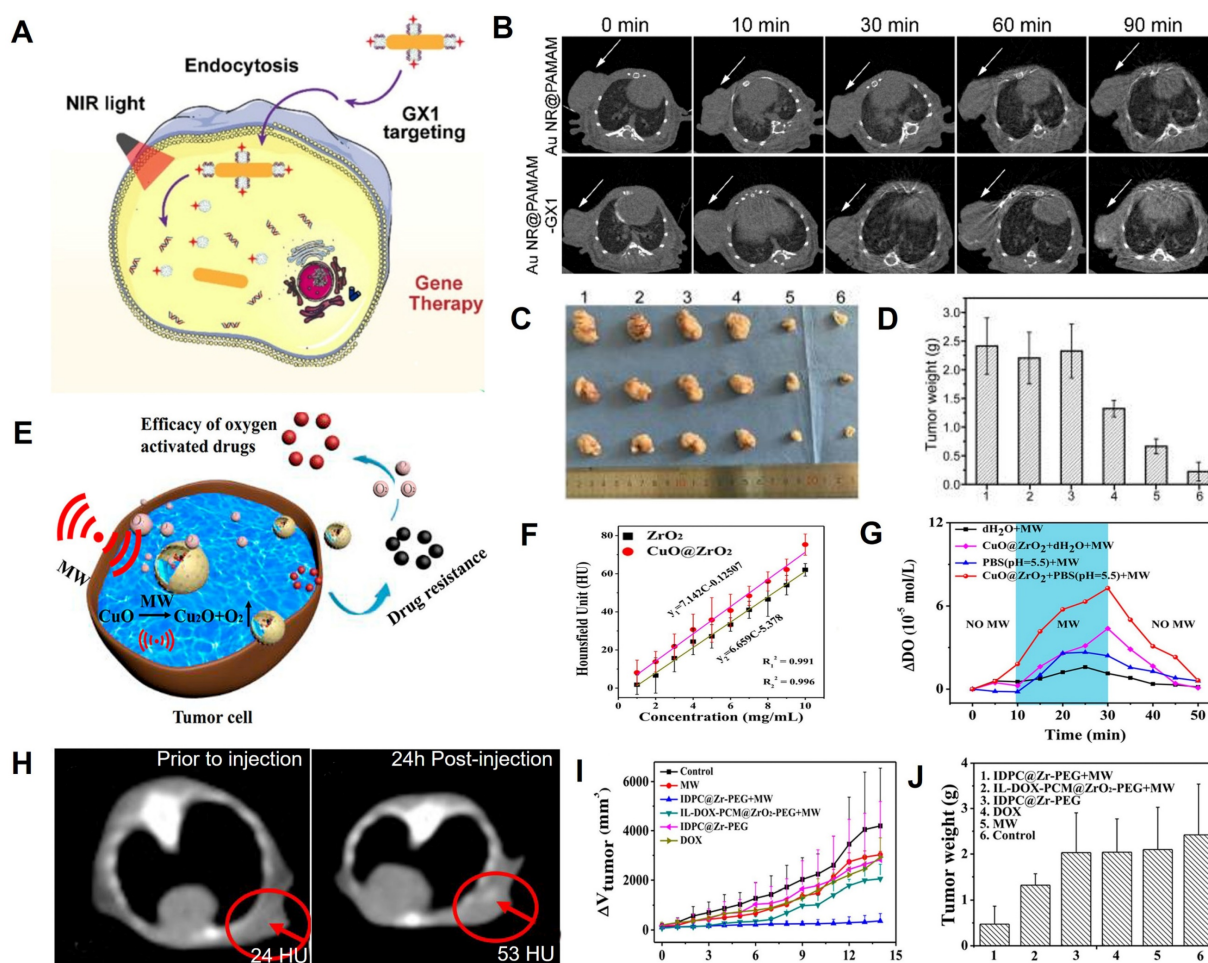


Figure 14. CT image-guided GT and MWTT. (A) Schematic illustration of FAM172A-mediated gene therapy. (B) Changes of CT contrast with time after injection. (C) Photographs of HCT-8 tumors at 14 days after different treatments. (D) Corresponding tumor weights. (E) Schematic illustration of IDPC@Zr-PEG for cancer treatment. (F) CT values of IDPC@Zr nanocomposites at different concentrations. (G) O₂-production capability of IDPC@Zr under MW irradiation. (H) CT images of the tumor at pre- and 24 h post-injection. (I) Tumor volume and (J) Tumor weight in different treatment groups at 14 days post-treatment. (A-D) Adapted with permission from [188], Copyright 2021 BioMed Central. (E-J) Adapted with permission from [190], Copyright 2018 American Chemical Society.

tumor was irradiated by MW at 24 h post-injection, and the tumor inhibition rate reached 92.14% after 14 days of treatment (**Figure 14I-J**). The results indicated that the CT image-guided MWTT provided a promising approach for clinical cancer therapy.

Conclusion and Outlook

CT imaging has evolved as an important tool for preclinical research and clinical applications. CT contrast agents are functional substances that can provide biomedical information by correlating imaging signals with molecular states or biological events *in vivo*, a prerequisite, and core technology for implementing accurate molecular imaging. Iodinated contrast agents, which account for 55% of total CT contrast agents, are widely used for diagnosing diseases and improving the resolution of CT images in soft tissues, particularly for identifying cancerous and normal tissues. However, iodinated contrast agents suffer from inherent drawbacks such as low contrast, short cycle times, and single function, making it challenging to meet the increasing clinical demands. Nanomaterial-based CT contrast agents have attracted much attention due to their various advantages, including homogeneous morphology, controllable size, high dispersion, excellent stability, and ease of functionalization. In particular, designing versatile nanomaterial-based CT contrast agents with comprehensive diagnostic and therapeutic capabilities has become a research hot spot.

Herein, we provide a comprehensive and up-to-date overview of recently reported studies on available CT contrast agents and their biomedical applications. CT contrast agents, such as Au-based nanomaterials, Bi-based nanomaterials, Ln-based nanomaterials, TM-based nanomaterials have been described. Regardless of various types, CT contrast agents can be used to CT image-guided therapy, including PTT, PDT, chemotherapy, gas therapy, RT, SDT, immunotherapy, starvation therapy, and synergistic therapy, among others.

Current research on the available CT contrast agents for cancer theranostics focuses on two main aspects: 1) designing multimodal imaging contrast agents and leveraging their complementary advantages to improve disease diagnosis accuracy and 2) integrating multiple functions into a single contrast agent, enabling the integration of diagnosis and treatment. Although there have been various reports on CT contrast agents in recent years, challenges remain in their design, large-scale preparation, cost, biocompatibility, potential toxicity, sensitivity, and specificity. Efforts should be devoted to addressing the following challenging issues:

1) Developing endogenous biomarker-

responsive CT contrast agents to improve sensitivity and specificity. Contrast agents are a central theme in CT imaging and are directly related to imaging quality. Therefore, harnessing biomarkers in the tumor microenvironment as stimulus-response units to design intelligent CT contrast agents is central to enhancing imaging contrast and improving the specificity and accuracy of disease diagnosis.

2) Although using CT contrast agents can enhance imaging contrast and improve diagnosis accuracy, only a few are currently available for use in the clinic due to their poor biocompatibility and potential toxicity. Optimizing the biological properties of contrast agents, such as stability, biocompatibility, toxicity, and targetability, to broaden their applications would be a promising research direction.

3) “All-in-one” theranostic nanoplatfoms for disease diagnosis and treatment have received increasing attention due to the integration of multiple functions and are expected to have the best chance of clinical success. Researchers should focus on utilizing contrast agents as an “all-in-one” nanotheranostic platform to allow real-time diagnosis and synchronous treatment. For example, AuNPs, with controllable size, easy surface modification, perfect radiosensitization capability, tunable optical properties, and high X-ray attenuation, can simultaneously realize multimodal (CT, MR, PA) image-guided synergistic treatment (RT, PTT) [191].

Abbreviations

ADCC: antibody-dependent cell-mediated cytotoxicity; AuNCs: gold nanocages; AuNPs: gold nanomaterials; AuNPrs: gold nanoprisms; AuNPTs: gold nanoplates; AuNRs: gold nanorods; AuNSs: gold nanostars; AuNShs: gold nanoshells; AuNSps: gold nanospheres; BiNPs: bismuth nanoparticles; BSA: bovine serum albumin; CDT: chemodynamic therapy; CPP: cell-penetrating peptide; CSS: core-shell-shell; CT: computed tomography; DOX: doxorubicin; DXL: docetaxel; EGFR: epidermal growth factor receptor; EMI: electric and musical industries; FA: folic acid; FR: folate receptor; GOD: glucose oxidase; GIT: gastrointestinal tract; GT: gene therapy; HA: hyaluronic acid; HIF: hypoxia-inducible factor; HU: Hounsfield unit; ICB: immune checkpoint blockade; LSPR: localized surface plasmon resonance; MPE: maximum permissible exposure; MRI: magnetic resonance imaging; MW: microwave; MWTT: microwave thermal therapy; NIR: near infrared; NGs: nanogels; NPs: nanoparticles; NRs: nanorods; NSs: nanosheets; PA: photoacoustic; PAA: polyacrylic acid; PCE: photothermal conversion efficiency; PCL: poly- ϵ -caprolactone; PDA: polydopamine; PDL1: programmed death ligand 1; α PDL1: programmed

death ligand 1 antibody; PDT: photodynamic therapy; PEG: polyethylene glycol; PEI: polyethylenimine; PFH: perfluorohexane; PL: photoluminescence; PSs: photosensitizers; PTAs: photothermal agents; PTT: photothermal therapy; PVA: polyvinyl alcohol; PVCL: poly(N-vinylcaprolactam); PVP: polyvinylpyrrolidone; RNS: reactive nitrogen species; RT: radiotherapy; SDT: sonodynamic therapy; SER: sensitization enhancement ratio; SPR: surface plasmon resonance; TM: transition metal; TME: tumor microenvironment; TPP: triphenylphosphine; US: ultrasound.

Acknowledgements

This work was supported by the National Natural Science Foundation of China (Grant Number: 91849209) and the Grants for Scientific Research of Distinguished Professor from Qingdao University, China (Grant Number: DC2200000953).

Competing Interests

The authors have declared that no competing interest exists.

References

- Pan X, Siewerdsen J, La Riviere P, Kalender W. Anniversary paper: development of X-ray computed tomography: the role of medical physics and AAPM from the 1970s to present. *Med Phys.* 2008; 35: 3728-39.
- Isherwood I. Sir Godfrey Hounsfield. *Radiology.* 2005; 234: 975-6.
- Kircher MF, Willmann JK. Molecular body imaging: MR imaging, CT, and US. part I. principles. *Radiology.* 2012; 263: 633-43.
- Samant P, Trevisi L, Ji X, Xiang L. X-ray induced acoustic computed tomography. *Photoacoustics.* 2020; 19: 100177.
- Kalender WA. X-ray computed tomography. *Phys Med Biol.* 2006; 51: R29-43.
- Goldman LW. Principles of CT and CT technology. *J Nucl Med Technol.* 2007; 35: 115-30.
- Yu SB, Watson AD. Metal-based X-ray contrast media. *Chem Rev.* 1999; 99: 2353-78.
- Lee N, Choi SH, Hyeon T. Nano-sized CT contrast agents. *Adv Mater.* 2013; 25: 2641-60.
- Riehemann K, Schneider SW, Luger TA, Godin B, Ferrari M, Fuchs H. Nanomedicine-challenge and perspectives. *Angew Chem Int Ed Engl.* 2009; 48: 872-97.
- Guerrero-Martinez A, Perez-Juste J, Liz-Marzan LM. Recent progress on silica coating of nanoparticles and related nanomaterials. *Adv Mater.* 2010; 22: 1182-95.
- Lusic H, Grinstaff MW. X-ray-computed tomography contrast agents. *Chem Rev.* 2013; 113: 1641-66.
- Singh J, Daftary A. Iodinated contrast media and their adverse reactions. *J Nucl Med Technol.* 2008; 36: 69-74.
- He W, Ai K, Lu L. Nanoparticulate X-ray CT contrast agents. *Sci China Chem.* 2015; 58: 753-60.
- Wang Z, Chen L, Chu Z, Huang C, Huang Y, Jia N. Gemcitabine-loaded gold nanospheres mediated by albumin for enhanced anti-tumor activity combining with CT imaging. *Mater Sci Eng C Mater Biol Appl.* 2018; 89: 106-18.
- Dou Y, Guo Y, Li X, Li X, Wang S, Wang L, et al. Size-tuning ionization to optimize gold nanoparticles for simultaneous enhanced CT imaging and radiotherapy. *ACS Nano.* 2016; 10: 2536-48.
- Hasannia M, Abnous K, Taghdisi SM, Nekooei S, Ramezani M, Alibolandi M. Synthesis of doxorubicin-loaded peptosomes hybridized with gold nanorod for targeted drug delivery and CT imaging of metastatic breast cancer. *J Nanobiotechnology.* 2022; 20: 391.
- Alkilany AM, Thompson LB, Boulos SP, Sisco PN, Murphy CJ. Gold nanorods: their potential for photothermal therapeutics and drug delivery, tempered by the complexity of their biological interactions. *Adv Drug Deliv Rev.* 2012; 64: 190-9.
- Qin J, Peng Z, Li B, Ye K, Zhang Y, Yuan F, et al. Gold nanorods as a theranostic platform for in vitro and in vivo imaging and photothermal therapy of inflammatory macrophages. *Nanoscale.* 2015; 7: 13991-4001.
- Lankveld DP, Rayavarapu RG, Krystek P, Oomen AG, Verharen HW, Leeuwen TGv, et al. Blood clearance and tissue distribution of PEGylated and non-PEGylated gold nanorods after intravenous administration in rats. *Nanomedicine.* 2011; 6: 339-49.
- Liu Y, Yuan H, Fales AM, Register JK, Vo-Dinh T. Multifunctional gold nanostars for molecular imaging and cancer therapy. *Front Chem.* 2015; 3: 51.
- Li D, Zhang Y, Wen S, Song Y, Tang Y, Zhu X, et al. Construction of polydopamine-coated gold nanostars for CT imaging and enhanced photothermal therapy of tumors: an innovative theranostic strategy. *J Mater Chem B.* 2016; 4: 4216-26.
- Wei P, Chen J, Hu Y, Li X, Wang H, Shen M, et al. Dendrimer-stabilized gold nanostars as a multifunctional theranostic nanoplatform for CT imaging, photothermal therapy, and gene silencing of tumors. *Adv Health Mater.* 2016; 5: 3203-13.
- Zhao Y, Liu W, Tian Y, Yang Z, Wang X, Zhang Y, et al. Anti-EGFR peptide-conjugated triangular gold nanoplates for computed tomography/photoacoustic imaging-guided photothermal therapy of non-small cell lung cancer. *ACS Appl Mater Interfaces.* 2018; 10: 16992-7003.
- Huang S, Liu Y, Xu X, Ji M, Li Y, Song C, et al. Triple therapy of hepatocellular carcinoma with microRNA-122 and doxorubicin co-loaded functionalized gold nanocages. *J Mater Chem B.* 2018; 6: 2217-29.
- You Q, Sun Q, Yu M, Wang J, Wang S, Liu L, et al. BSA-bioinspired gadolinium hybrid-functionalized hollow gold nanoshells for NIRF/PA/CT/MR quadmodal diagnostic imaging-guided photothermal/photodynamic cancer therapy. *ACS Appl Mater Interfaces.* 2017; 9: 40017-30.
- Liu W, Liu K, Zhao Y, Zhao S, Luo S, Tian Y, et al. T₁-weighted MR/CT dual-modality imaging-guided photothermal therapy using gadolinium-functionalized triangular gold nanoprism. *RSC Adv.* 2017; 7: 15702-8.
- Cui X, Qin F, Ruan Q, Zhuo X, Wang J. Circular gold nanodisks with synthetically tunable diameters and thicknesses. *Adv Funct Mater.* 2018; 28: 1705516.
- Ross RD, Cole LE, Tilley JMR, Roeder RK. Effects of functionalized gold nanoparticle size on X-ray attenuation and substrate binding affinity. *Chem Mater.* 2014; 26: 1187-94.
- Dong YC, Hajfathalian M, Maidment PSN, Hsu JC, Naha PC, Si-Mohamed S, et al. Effect of gold nanoparticle size on their properties as contrast agents for computed tomography. *Sci Rep.* 2019; 9: 14912.
- Tsvirkun D, Ben-Nun Y, Merquiol E, Zlotver I, Meir K, Weiss-Sadan T, et al. CT imaging of enzymatic activity in cancer using covalent probes reveal a size-dependent pattern. *J Am Chem Soc.* 2018; 140: 12010-20.
- Fan W, Peng H, Yu Z, Wang L, He H, Ma Y, et al. The long-circulating effect of pegylated nanoparticles revisited via simultaneous monitoring of both the drug payloads and nanocarriers. *Acta Pharm Sin B.* 2022; 12: 2479-93.
- Qu X, Li X, Liang J, Wang Y, Liu M, Liang J. Micro-CT imaging of RGD-conjugated gold nanorods targeting tumor in vivo. *J Nanomater.* 2016; 2016: 8368154.
- Shi P, Qu K, Wang J, Li M, Ren J, Qu X. pH-responsive NIR enhanced drug release from gold nanocages possesses high potency against cancer cells. *Chem Commun (Camb).* 2012; 48: 7640-2.
- Chen J, Glaus C, Laforest R, Zhang Q, Yang M, Gidding M, et al. Gold nanocages as photothermal transducers for cancer treatment. *Small.* 2010; 6: 811-7.
- Wang Z, Chen Z, Liu Z, Shi P, Dong K, Ju E, et al. A multi-stimuli responsive gold nanocage-hyaluronic platform for targeted photothermal and chemotherapy. *Biomaterials.* 2014; 35: 9678-88.
- Bao S, Huang S, Liu Y, Hu Y, Wang W, Ji M, et al. Gold nanocages with dual modality for image-guided therapeutics. *Nanoscale.* 2017; 9: 7284-96.
- Huang S, Duan S, Wang J, Bao S, Qiu X, Li C, et al. Folic-acid-mediated functionalized gold nanocages for targeted delivery of anti-miR-181b in combination of gene therapy and photothermal therapy against hepatocellular carcinoma. *Adv Funct Mater.* 2016; 26: 2532-44.
- Fu Q, Zhu R, Song J, Yang H, Chen X. Photoacoustic imaging: contrast agents and their biomedical applications. *Adv Mater.* 2019; 31: 1805875.
- Moore C, Jocker JV. Strategies for image-guided therapy, surgery, and drug delivery using photoacoustic imaging. *Theranostics.* 2019; 9: 1550-71.
- An J, Yang XQ, Cheng K, Song XL, Zhang L, Li C, et al. In vivo computed tomography/photoacoustic imaging and NIR-triggered chemo-photothermal combined therapy based on a gold nanostar-, mesoporous silica-, and thermosensitive liposome-composited nanoprobe. *ACS Appl Mater Interfaces.* 2017; 9: 41748-59.
- Fu Q, Li Z, Fu F, Chen X, Song J, Yang H. Stimuli-responsive plasmonic assemblies and their biomedical applications. *Nano Today.* 2021; 36: 101014.
- Lane IA, Qian X, Nie S. SERS nanoparticles in medicine: from label-free detection to spectroscopic tagging. *Chem Rev.* 2015; 115: 10489-529.
- Wang M, Chang M, Chen Q, Wang D, Li C, Hou Z, et al. Au₂Pt-PEG-Ce6 nanoformulation with dual nanozyme activities for synergistic chemodynamic therapy/phototherapy. *Biomaterials.* 2020; 252: 120093.
- Smith BR, Gambhir SS. Nanomaterials for in vivo imaging. *Chem Rev.* 2017; 117: 901-86.
- Hu DH, Sheng ZH, Zhang PF, Yang DZ, Liu SH, Gong P, et al. Hybrid gold-gadolinium nanoclusters for tumor-targeted NIRF/CT/MRI triple-modal imaging in vivo. *Nanoscale.* 2013; 5: 1624-8.

46. Xue S, Wang Y, Wang M, Zhang L, Du X, Gu H, et al. Iodinated oil-loaded, fluorescent mesoporous silica-coated iron oxide nanoparticles for magnetic resonance imaging/computed tomography/fluorescence trimodal imaging. *Int J Nanomedicine*. 2014; 9: 2527-38.
47. Yu C, Bao H, Chen Z, Li X, Liu X, Wang W, et al. Enhanced and long-term CT imaging tracking of transplanted stem cells labeled with temperature-responsive gold nanoparticles. *J Mater Chem B*. 2021; 9: 2854-65.
48. Yu C, Chen Z, Li X, Bao H, Wang Y, Zhang B, et al. pH-triggered aggregation of gold nanoparticles for enhanced labeling and long-term CT imaging tracking of stem cells in pulmonary fibrosis treatment. *Small*. 2021; 17: e2101861.
49. Bouche M, Puhlinger M, Iturmendi A, Amirshaghghi A, Tsourkas A, Teasdale I, et al. Activatable hybrid polyphosphazene-AuNP nanoprobe for ROS detection by bimodal PA/CT imaging. *ACS Appl Mater Interfaces*. 2019; 11: 28648-56.
50. Iturmendi A, Monkowius U, Teasdale I. Oxidation responsive polymers with a triggered degradation via arylboronate self-immolative motifs on a polyphosphazene backbone. *ACS Macro Lett*. 2017; 6: 150-4.
51. Li H, Sun H. Recent advances in bioinorganic chemistry of bismuth. *Curr Opin Chem Biol*. 2012; 16: 74-83.
52. Glen G, Briand, Burford N. Bismuth compounds and preparations with biological or medicinal relevance. *Chem Rev*. 1999; 99: 2601-58.
53. Swy ER, Schwartz-Duval AS, Shuboni DD, Latourette MT, Mallet CL, Parys M, et al. Dual-modality, fluorescent, PLGA encapsulated bismuth nanoparticles for molecular and cellular fluorescence imaging and computed tomography. *Nanoscale*. 2014; 6: 13104-12.
54. Wei B, Zhang X, Zhang C, Jiang Y, Fu YY, Yu C, et al. Facile synthesis of uniform-sized bismuth nanoparticles for CT visualization of gastrointestinal tract in vivo. *ACS Appl Mater Interfaces*. 2016; 8: 12720-6.
55. Mao F, Wen L, Sun C, Zhang S, Wang G, Zeng J, et al. Ultrasmall biocompatible Bi₂Se₃ nanodots for multimodal imaging-guided synergistic radiophotothermal therapy against cancer. *ACS Nano*. 2016; 10: 11145-55.
56. Rabin O, Manuel Perez J, Grimm J, Wojtkiewicz G, Weissleder R. An X-ray computed tomography imaging agent based on long-circulating bismuth sulphide nanoparticles. *Nat Mater*. 2006; 5: 118-22.
57. Chen J, Yang XQ, Meng YZ, Huang HH, Qin MY, Yan DM, et al. CT imaging using bismuth sulfide modified with a highly biocompatible Pluronic F127. *Nanotechnology*. 2014; 25: 295103.
58. Wang Y, Wu Y, Liu Y, Shen J, Lv L, Li L, et al. BSA-mediated synthesis of bismuth sulfide nanotheranostic agents for tumor multimodal imaging and thermoradiotherapy. *Adv Funct Mater*. 2016; 26: 5335-44.
59. Cheng Y, Chang Y, Feng Y, Jian H, Wu X, Zheng R, et al. Bismuth sulfide nanorods with retractable zinc protoporphyrin molecules for suppressing innate antioxidant defense system and strengthening phototherapeutic effects. *Adv Mater*. 2019; 31: e1806808.
60. Zhou D, Li C, He M, Ma M, Li P, Gong Y, et al. Folate-targeted perfluorohexane nanoparticles carrying bismuth sulfide for use in US/CT dual-mode imaging and synergistic high-intensity focused ultrasound ablation of cervical cancer. *J Mater Chem B*. 2016; 4: 4164-81.
61. Kinsella JM, Jimenez RE, Karmali PP, Rush AM, Kotamraju VR, Gianneschi NC, et al. X-ray computed tomography imaging of breast cancer by using targeted peptide-labeled bismuth sulfide nanoparticles. *Angew Chem Int Ed Engl*. 2011; 50: 12308-11.
62. Zhang P, Wang L, Chen X, Li X, Yuan Q. Ultrasmall PEI-decorated Bi₂Se₃ nanodots as a multifunctional theranostic nanoplatform for in vivo CT imaging-guided cancer photothermal therapy. *Front Pharmacol*. 2021; 12: 795012.
63. Hu X, Sun J, Li F, Li R, Wu J, He J, et al. Renal-clearable hollow bismuth subcarbonate nanotubes for tumor targeted computed tomography imaging and chemoradiotherapy. *Nano Lett*. 2018; 18: 1196-204.
64. Du F, Lou J, Jiang R, Fang Z, Zhao X, Niu Y, et al. Hyaluronic acid-functionalized bismuth oxide nanoparticles for computed tomography imaging-guided radiotherapy of tumor. *Int J Nanomedicine*. 2017; 12: 5973-92.
65. Liu J, Wang P, Zhang X, Wang L, Wang D, Gu Z, et al. Rapid degradation and high renal clearance of Cu₃Bi₂S₇ nanodots for efficient cancer diagnosis and photothermal therapy in vivo. *ACS Nano*. 2016; 10: 4587-98.
66. Guo Z, Zhu S, Yong Y, Zhang X, Dong X, Du J, et al. Synthesis of BSA-coated BiO/Bi₂S₃ semiconductor heterojunction nanoparticles and their applications for radio/photodynamic/photothermal synergistic therapy of tumor. *Adv Mater*. 2017; 29: 1704136.
67. Ahmad MW, Xu W, Kim SJ, Baek JS, Chang Y, Bae JE, et al. Potential dual imaging nanoparticle: Gd₂O₃ nanoparticle. *Sci Rep*. 2015; 5: 8549.
68. Ghazanfari A, Marasini S, Miao X, Park JA, Jung KH, Ahmad MY, et al. Synthesis, characterization, and X-ray attenuation properties of polyacrylic acid-coated ultrasmall heavy metal oxide (Bi₂O₃, Yb₂O₃, NaTaO₃, Dy₂O₃, and Gd₂O₃) nanoparticles as potential CT contrast agents. *Colloids Surf A Physicochem Eng Asp*. 2019; 576: 73-81.
69. Lee EJ, Heo WC, Park JW, Chang Y, Bae JE, Chae KS, et al. D-glucuronic acid coated Gd(IO₃)₃·2H₂O nanomaterial as a potential T₁ MRI-CT dual contrast agent. *Eur J Inorg Chem*. 2013; 2013: 2858-66.
70. Olifirenko V, Abduraimova A, Kang MS, Raja IS, Duisenbayeva B, Molkenova A, et al. Potential applicability of polyethyleneimine PEI-coated Eu₂O₃ and Dy₂O₃ nanoparticles for contrast enhancement in computed tomography. *Nano Express*. 2021; 2: 010022.
71. Jia T, Xu J, Dong S, He F, Zhong C, Yang G, et al. Mesoporous cerium oxide-coated upconversion nanoparticles for tumor-responsive chemo-photodynamic therapy and bioimaging. *Chem Sci*. 2019; 10: 8618-33.
72. Naha PC, Hsu JC, Kim J, Shah S, Bouche M, Si-Mohamed S, et al. Dextran-coated cerium oxide nanoparticles: a computed tomography contrast agent for imaging the gastrointestinal tract and inflammatory bowel disease. *ACS Nano*. 2020; 14: 10187-97.
73. Cheung ENM, Alvares RDA, Oakden W, Chaudhary R, Hill ML, Pichaandi J, et al. Polymer-stabilized lanthanide fluoride nanoparticle aggregates as contrast agents for magnetic resonance imaging and computed tomography. *Chem Mater*. 2010; 22: 4728-39.
74. Ni D, Zhang J, Bu W, Zhang C, Yao Z, Xing H, et al. PEGylated NaHoF₄ nanoparticles as contrast agents for both X-ray computed tomography and ultra-high field magnetic resonance imaging. *Biomaterials*. 2016; 76: 218-25.
75. Tse JJ, Dunmore-Buyze PJ, Drangova M, Holdsworth DW. Erbium-based perfusion contrast agent for small-animal microvessel imaging. *Contrast Media Mol Imaging*. 2017; 2017: 7368384.
76. Cruje C, Dunmore-Buyze J, MacDonald JP, Holdsworth DW, Drangova M, Gillies ER. Polymer assembly encapsulation of lanthanide nanoparticles as contrast agents for in vivo micro-CT. *Biomacromolecules*. 2018; 19: 896-905.
77. Xiong L, Yang T, Yang Y, Xu C, Li F. Long-term in vivo biodistribution imaging and toxicity of polyacrylic acid-coated upconversion nanophosphors. *Biomaterials*. 2010; 31: 7078-85.
78. Liu Y, Ai K, Liu J, Yuan Q, He Y, Lu L. A high-performance ytterbium-based nanoparticulate contrast agent for in vivo X-ray computed tomography imaging. *Angew Chem Int Ed Engl*. 2012; 51: 1437-42.
79. Wang F, Banerjee D, Liu Y, Chen X, Liu X. Upconversion nanoparticles in biological labeling, imaging, and therapy. *Analyst*. 2010; 135: 1839-54.
80. Zhou J, Liu Z, Li F. Upconversion nanophosphors for small-animal imaging. *Chem Soc Rev*. 2012; 41: 1323-49.
81. Zhu X, Zhou J, Chen M, Shi M, Feng W, Li F. Core-shell Fe₃O₄@NaLuF₄:Yb,Er/Tm nanostructure for MRI, CT and upconversion luminescence tri-modality imaging. *Biomaterials*. 2012; 33: 4618-27.
82. Zhou J, Zhu X, Chen M, Sun Y, Li F. Water-stable NaLuF₄-based upconversion nanophosphors with long-term validity for multimodal lymphatic imaging. *Biomaterials*. 2012; 33: 6201-10.
83. Dai Y, Yang D, Yu D, Cao C, Wang Q, Xie S, et al. Mussel-inspired polydopamine-coated lanthanide nanoparticles for NIR-II/CT dual imaging and photothermal therapy. *ACS Appl Mater Interfaces*. 2017; 9: 26674-83.
84. Luo L, Shu R, Wu A. Nanomaterial-based cancer immunotherapy. *J Mater Chem B*. 2017; 5: 5517-31.
85. Zhong X, Wang X, Zhan G, Tang Y, Yao Y, Dong Z, et al. NaCeF₄:Gd,Tb scintillator as an X-ray responsive photosensitizer for multimodal imaging-guided synchronous radio/radiodynamic therapy. *Nano Lett*. 2019; 19: 8234-44.
86. He S, Johnson NJJ, Nguyen Huu VA, Cory E, Huang Y, Sah RL, et al. Simultaneous enhancement of photoluminescence, MRI relaxivity, and CT contrast by tuning the interfacial layer of lanthanide heteroepitaxial nanoparticles. *Nano Lett*. 2017; 17: 4873-80.
87. Julie Marill, Naemunnisa Mohamed Anesary, Ping Zhang, Sonia Vivet, Elsa Borghi, Laurent Levy, et al. Hafnium oxide nanoparticles: toward an in vitro predictive biological effect? *Radiat Oncol*. 2014; 9: 150.
88. Roessler AC, Hupfer M, Kolditz D, Jost G, Pietsch H, Kalender WA. High atomic number contrast media offer potential for radiation dose reduction in contrast-enhanced computed tomography. *Invest Radiol*. 2016; 51: 249-54.
89. McGinnity TL, Dominguez O, Curtis TE, Nallathambi PD, Hoffman AJ, Roeder RK. Hafnia (HfO₂) nanoparticles as an X-ray contrast agent and mid-infrared biosensor. *Nanoscale*. 2016; 8: 13627-37.
90. Song G, Chen Y, Liang C, Yi X, Liu J, Sun X, et al. Catalase-loaded TaOx nanoshells as bio-nanoreactors combining high-Z element and enzyme delivery for enhancing radiotherapy. *Adv Mater*. 2016; 28: 7143-8.
91. Bonitatibus PJ, Jr., Torres AS, Goddard GD, FitzGerald PF, Kulkarni AM. Synthesis, characterization, and computed tomography imaging of a tantalum oxide nanoparticle imaging agent. *Chem Commun (Camb)*. 2010; 46: 8956-8.
92. Oh MH, Lee N, Kim H, Park SP, Piao Y, Lee J, et al. Large-scale synthesis of bioinert tantalum oxide nanoparticles for X-ray computed tomography imaging and bimodal image-guided sentinel lymph node mapping. *J Am Chem Soc*. 2011; 133: 5508-15.
93. Liu Y, Ji X, Liu J, Tong WWL, Askhatova D, Shi J. Tantalum sulfide nanosheets as a theranostic nanoplatform for computed tomography imaging-guided combinatorial chemo-photothermal therapy. *Adv Funct Mater*. 2017; 27: 1703261.
94. Zhou Z, Kong B, Yu C, Shi X, Wang M, Liu W, et al. Tungsten oxide nanorods: an efficient nanoplatform for tumor CT imaging and photothermal therapy. *Sci Rep*. 2014; 4: 3653.
95. Dong K, Liu Z, Liu J, Huang S, Li Z, Yuan Q, et al. Biocompatible and high-performance amino acids-capped MnWO₄ nanocasting as a novel non-lanthanide contrast agent for X-ray computed tomography and T₁-weighted magnetic resonance imaging. *Nanoscale*. 2014; 6: 2211-7.
96. Jakhmola A, Anton N, Anton H, Messaddeq N, Hallouard F, Klymchenko A, et al. Poly-epsilon-caprolactone tungsten oxide nanoparticles as a contrast agent for X-ray computed tomography. *Biomaterials*. 2014; 35: 2981-6.
97. Tian G, Zhang X, Zheng X, Yin W, Ruan L, Liu X, et al. Multifunctional Rb₂WO₆ nanorods for simultaneous combined chemo-photothermal therapy and photoacoustic/CT imaging. *Small*. 2014; 10: 4160-70.

98. Shen S, Chao Y, Dong Z, Wang G, Yi X, Song G, et al. Bottom-up preparation of uniform ultrathin rhenium disulfide nanosheets for image-guided photothermal radiotherapy. *Adv Funct Mater.* 2017; 27: 1700250.
99. Miao ZH, Lv LX, Li K, Liu PY, Li Z, Yang H, et al. Liquid exfoliation of colloidal rhenium disulfide nanosheets as a multifunctional theranostic agent for in vivo photoacoustic/CT imaging and photothermal therapy. *Small.* 2018; 14: e1703789.
100. Marbella LE, Millstone JE. NMR techniques for noble metal nanoparticles. *Chem Mater.* 2015; 27: 2721-39.
101. Yim G, Kang S, Kim YJ, Kim YK, Min DH, Jang H. Hydrothermal galvanic-replacement-tethered synthesis of Ir-Ag-IrO₂ nanoplates for computed tomography-guided multiwavelength potent thermodynamic cancer therapy. *ACS Nano.* 2019; 13: 3434-47.
102. Tang Y, Yang T, Wang Q, Lv X, Song X, Ke H, et al. Albumin-coordinated assembly of clearable platinum nanodots for photo-induced cancer theranostics. *Biomaterials.* 2018; 154: 248-60.
103. Wang Q, Wang H, Yang Y, Jin L, Liu Y, Wang Y, et al. Plasmonic Pt superstructures with boosted near-infrared absorption and photothermal conversion efficiency in the second biowindow for cancer therapy. *Adv Mater.* 2019; 31: e1904836.
104. Wang Z, Chen L, Huang C, Huang Y, Jia N. Albumin-mediated platinum nanocrystals for in vivo enhanced computed tomography imaging. *J Mater Chem B.* 2017; 5: 3498-510.
105. Yan Y, Yang C, Dai G, Zhang Y, Tu G, Li Y, et al. Folic acid-conjugated CuFeSe₂ nanoparticles for targeted T₂-weighted magnetic resonance imaging and computed tomography of tumors in vivo. *Int J Nanomedicine.* 2021; 16: 6429-40.
106. Zhang X, Yao M, Chen M, Li L, Dong C, Hou Y, et al. Hyaluronic acid-coated silver nanoparticles as a nanopatform for in vivo imaging applications. *ACS Appl Mater Interfaces.* 2016; 8: 25650-3.
107. Abdel-Mohsen AM, Hrdina R, Burgert L, Krylova G, Abdel-Rahman RM, Krejcová A, et al. Green synthesis of hyaluronan fibers with silver nanoparticles. *Carbohydr Polym.* 2012; 89: 411-22.
108. Li Z, Tan S, Li S, Shen Q, Wang K. Cancer drug delivery in the nano era: An overview and perspectives (Review). *Oncol Rep.* 2017; 38: 611-24.
109. Kalbasi A, Komar C, Tooker GM, Liu M, Lee JW, Gladney WL, et al. Tumor-derived CCL2 mediates resistance to radiotherapy in pancreatic ductal adenocarcinoma. *Clin Cancer Res.* 2017; 23: 137-48.
110. Bray FN, Simmons BJ, Wolfson AH, Nouri K. Acute and Chronic Cutaneous Reactions to Ionizing Radiation Therapy. *Dermatol Ther (Heidelb).* 2016; 6: 185-206.
111. Beik J, Abed Z, Ghoreishi FS, Hosseini-Nami S, Mehrzadi S, Shakeri-Zadeh A, et al. Nanotechnology in hyperthermia cancer therapy: From fundamental principles to advanced applications. *J Control Release.* 2016; 235: 205-21.
112. Fernandes N, Rodrigues CF, Moreira AF, Correia IJ. Overview of the application of inorganic nanomaterials in cancer photothermal therapy. *Biomater Sci.* 2020; 8: 2990-3020.
113. Cihoric N, Tsikkinis A, van Rhooen G, Crezee H, Aebersold DM, Bodis S, et al. Hyperthermia-related clinical trials on cancer treatment within the ClinicalTrials.gov registry. *Int J Hyperthermia.* 2015; 31: 609-14.
114. Gai S, Yang G, Yang P, He F, Lin J, Jin D, et al. Recent advances in functional nanomaterials for light-triggered cancer therapy. *Nano Today.* 2018; 19: 146-87.
115. Mocan T, Matea CT, Cojocaru I, Ilie I, Tabaran FA, Zaharie F, et al. Photothermal treatment of human pancreatic cancer using PEGylated multi-walled carbon nanotubes induces apoptosis by triggering mitochondrial membrane depolarization mechanism. *J Cancer.* 2014; 5: 679-88.
116. Jung HS, Verwilt P, Sharma A, Shin J, Sessler JL, Kim JS. Organic molecule-based photothermal agents: An expanding photothermal therapy universe. *Chem Soc Rev.* 2018; 47: 2280-97.
117. Adams S, Zhang JZ. Unique optical properties and applications of hollow gold nanospheres (HGNS). *Coord Chem Rev.* 2016; 320-321: 18-37.
118. Yang H, He H, Tong Z, Xia H, Mao Z, Gao C. The impact of size and surface ligand of gold nanorods on liver cancer accumulation and photothermal therapy in the second near-infrared window. *J Colloid Interface Sci.* 2020; 565: 186-96.
119. Xu Y, Wang X, Cheng L, Liu Z, Zhang Q. High-yield synthesis of gold bipyramids for in vivo CT imaging and photothermal cancer therapy with enhanced thermal stability. *Chem Eng J.* 2019; 378: 122025.
120. Tian Y, Luo S, Yan H, Teng Z, Pan Y, Zeng L, et al. Gold nanostars functionalized with amine-terminated PEG for X-ray/CT imaging and photothermal therapy. *J Mater Chem B.* 2015; 3: 4330-7.
121. Liu B, Li C, Cheng Z, Hou Z, Huang S, Lin J. Functional nanomaterials for near-infrared-triggered cancer therapy. *Biomater Sci.* 2016; 4: 890-909.
122. Thomas RJ, Rockwell BA, Marshall WJ, Aldrich RC, Zimmerman SA, Rockwell RJ. A procedure for laser hazard classification under the Z136.1-2000 American National Standard for Safe Use of Lasers. *J Laser Appl.* 2002; 14: 57-66.
123. Cui J, Jiang R, Guo C, Bai X, Xu S, Wang L. Fluorine grafted Cu₇S₄-Au heterodimers for multimodal imaging guided photothermal therapy with high penetration depth. *J Am Chem Soc.* 2018; 140: 5890-4.
124. Liu Y, Zhen W, Wang Y, Liu J, Jin L, Zhang T, et al. One-dimensional Fe₂P acts as a fenton agent in response to NIR II light and ultrasound for deep tumor synergistic theranostics. *Angew Chem Int Ed Engl.* 2019; 58: 2407-12.
125. Li X, Lee S, Yoon J. Supramolecular photosensitizers rejuvenate photodynamic therapy. *Chem Soc Rev.* 2018; 47: 1174-88.
126. Gupta SC, Hevia D, Patchva S, Park B, Koh W, Aggarwal BB. Upsides and downsides of reactive oxygen species for cancer: the roles of reactive oxygen species in tumorigenesis, prevention, and therapy. *Antioxid Redox Signal.* 2011; 16: 1295-322.
127. Fu Q, Yu L, Wang Y, Li P, Song J. Biomarker-responsive nanosystems for chronic disease theranostics. *Adv Funct Mater.* 2022; doi:10.1002/adfm.202206300.
128. Zhang L, Yang XQ, Wei JS, Li X, Wang H, Zhao YD. Intelligent gold nanostars for in vivo CT imaging and catalase-enhanced synergistic photodynamic & photothermal tumor therapy. *Theranostics.* 2019; 9: 5424-42.
129. Lan M, Zhao S, Liu W, Lee CS, Zhang W, Wang P. Photosensitizers for photodynamic therapy. *Adv Healthc Mater.* 2019; 8: e1900132.
130. Chen MM, Hao HL, Zhao W, Zhao X, Chen HY, Xu JJ. A plasmon-enhanced theranostic nanopatform for synergistic chemo-phototherapy of hypoxic tumors in the NIR-II window. *Chem Sci.* 2021; 12: 10848-54.
131. Senapati S, Mahanta AK, Kumar S, Maiti P. Controlled drug delivery vehicles for cancer treatment and their performance. *Signal Transduct Target Ther.* 2018; 3: 7.
132. Wang Y, Song S, Liu J, Liu D, Zhang H. ZnO-functionalized upconverting nanotheranostic agent: multi-modality imaging-guided chemotherapy with on-demand drug release triggered by pH. *Angew Chem Int Ed Engl.* 2015; 54: 536-40.
133. Wang Y, Shim MS, Levinson NS, Sung HW, Xia Y. Stimuli-responsive materials for controlled release of theranostic agents. *Adv Funct Mater.* 2014; 24: 4206-20.
134. Li WQ, Guo HF, Li LY, Zhang YF, Cui JW. The promising role of antibody drug conjugate in cancer therapy: Combining targeting ability with cytotoxicity effectively. *Cancer Med.* 2021; 10: 4677-96.
135. Liu M, Wang L, Lo Y, Shiu SC, Kinghorn AB, Tanner JA. Aptamer-enabled nanomaterials for therapeutics, drug targeting and imaging. *Cells.* 2022; 11: 159.
136. Huang H, Yang DP, Liu M, Wang X, Zhang Z, Zhou G, et al. pH-sensitive Au-BSA-DOX-FA nanocomposites for combined CT imaging and targeted drug delivery. *Int J Nanomedicine.* 2017; 12: 2829-43.
137. Taheri-Ledari R, Zhang W, Radmanesh M, Mirmohammadi SS, Maleki A, Cathcart N, et al. Multi-stimuli nanocomposite therapeutic: docetaxel targeted delivery and synergies in treatment of human breast cancer tumor. *Small.* 2020; 16: e2002733.
138. He S, Li C, Zhang Q, Ding J, Liang XJ, Chen X, et al. Tailoring platinum(IV) amphiphiles for self-targeting all-in-One assemblies as precise multimodal theranostic nanomedicine. *ACS Nano.* 2018; 12: 7272-81.
139. Pabla N, Dong Z. Cisplatin nephrotoxicity: mechanisms and renoprotective strategies. *Kidney Int.* 2008; 73: 994-1007.
140. Yu J, He X, Zhang Q, Zhou D, Wang Z, Huang Y. Iodine conjugated Pt(IV) nanoparticles for precise chemotherapy with iodine-Pt guided computed tomography imaging and biotin-mediated tumor-targeting. *ACS Nano.* 2022; 16: 6835-46.
141. Barton MB, Jacob S, Shafiq J, Wong K, Thompson SR, Hanna TP, et al. Estimating the demand for radiotherapy from the evidence: a review of changes from 2003 to 2012. *Radiother Oncol.* 2014; 112: 140-4.
142. Wang H, Mu X, He H, Zhang XD. Cancer radiosensitizers. *Trends Pharmacol Sci.* 2018; 39: 24-48.
143. Willers H, Azzoli CG, Santivasi WL, Xia F. Basic mechanisms of therapeutic resistance to radiation and chemotherapy in lung cancer. *J Cancer.* 2013; 19: 200-7.
144. Schuemann J, Berbeco R, Chithrani DB, Cho SH, Kumar R, McMahon SJ, et al. Roadmap to clinical use of gold nanoparticles for radiation sensitization. *Int J Radiat Oncol Biol Phys.* 2016; 94: 189-205.
145. Luan S, Xie R, Yang Y, Xiao X, Zhou J, Li X, et al. Acid-responsive aggregated gold nanoparticles for radiosensitization and synergistic chemoradiotherapy in the treatment of esophageal cancer. *Small.* 2022; 18: e2200115.
146. Retif P, Pinel S, Toussaint M, Frochot C, Chouikrat R, Bastogne T, et al. Nanoparticles for radiation therapy enhancement: the key parameters. *Theranostics.* 2015; 5: 1030-44.
147. Brown JM, Wilson WR. Exploiting tumour hypoxia in cancer treatment. *Nat Rev Cancer.* 2004; 4: 437-47.
148. Shen Z, Xia J, Ma Q, Zhu W, Gao Z, Han S, et al. Tumor microenvironment-triggered nanosystems as dual-relief tumor hypoxia immunomodulators for enhanced phototherapy. *Theranostics.* 2020; 10: 9132-52.
149. Wang D, Xue B, Ohulchanskyy TY, Liu Y, Yakovliev A, Ziniuk R, et al. Inhibiting tumor oxygen metabolism and simultaneously generating oxygen by intelligent upconversion nanotherapeutics for enhanced photodynamic therapy. *Biomaterials.* 2020; 251: 120088.
150. Zhu J, Xiao T, Zhang J, Che H, Shi Y, Shi X, et al. Surface-charge-switchable nanoclusters for magnetic resonance imaging-guided and glutathione depletion-enhanced photodynamic therapy. *ACS Nano.* 2020; 14: 11225-37.
151. Zhang C, Tu W, Chen X, Xu B, Li X, Hu C, et al. Intelligent design of polymer nanogels for full-process sensitized radiotherapy and dual-mode computed tomography/magnetic resonance imaging of tumors. *Theranostics.* 2022; 12: 3420-37.

152. Hossain M, Su M. Nanoparticle location and material dependent dose enhancement in X-ray radiation therapy. *J Phys Chem C Nanomater Interfaces*. 2012; 116: 23047-52.
153. Hao Y, Peng B, Si C, Wang B, Luo C, Chen M, et al. PVP-modified multifunctional Bi₂WO₆ nanosheets for enhanced CT imaging and cancer radiotherapy. *ACS Omega*. 2022; 7: 18795-803.
154. Carter BW, Bhosale PR, Yang WT. Immunotherapy and the role of imaging. *Cancer*. 2018; 124: 2906-22.
155. Li W, Wei H, Li H, Gao J, Feng S-S, Guo Y. Cancer nanoimmunotherapy using advanced pharmaceutical nanotechnology. *Nanomedicine*. 2014; 9: 2587-605.
156. Seth A, Oh D-B, Lim YT. Nanomaterials for enhanced immunity as an innovative paradigm in nanomedicine. *Nanomedicine*. 2015; 10: 959-75.
157. Jiao P, Otto M, Geng Q, Li C, Li F, Butch ER, et al. Enhancing both CT imaging and natural killer cell-mediated cancer cell killing by a GD2-targeting nanoconstruct. *J Mater Chem B*. 2016; 4: 513-20.
158. Shi J, Kantoff PW, Wooster R, Farokhzad OC. Cancer nanomedicine: progress, challenges and opportunities. *Nat Rev Cancer*. 2017; 17: 20-37.
159. Guo L, Zhang H, Chen B. Nivolumab as programmed death-1 (PD-1) inhibitor for targeted immunotherapy in tumor. *J Cancer*. 2017; 8: 410-6.
160. Force J, Salama AK. First-line treatment of metastatic melanoma: role of nivolumab. *Immunotargets Ther*. 2017; 6: 1-10.
161. Phillips GK, Atkins M. Therapeutic uses of anti-PD-1 and anti-PD-L1 antibodies. *Int Immunol*. 2015; 27: 39-46.
162. Mahmoudi M, Farokhzad OC. Cancer immunotherapy: Wound-bound checkpoint blockade. *Nat Biomed Eng*. 2017; 1: 0031.
163. Meir R, Shamalov K, Sadan T, Motiei M, Yaari G, Cohen CJ, et al. Fast image-guided stratification using anti-programmed death ligand 1 gold nanoparticles for cancer immunotherapy. *ACS Nano*. 2017; 11: 11127-34.
164. Yu S, Chen Z, Zeng X, Chen X, Gu Z. Advances in nanomedicine for cancer starvation therapy. *Theranostics*. 2019; 9: 8026-47.
165. Li S, Jiang Q, Liu S, Zhang Y, Tian Y, Song C, et al. A DNA nanorobot functions as a cancer therapeutic in response to a molecular trigger in vivo. *Nat Biotechnol*. 2018; 36: 258-64.
166. Fu LH, Qi C, Lin J, Huang P. Catalytic chemistry of glucose oxidase in cancer diagnosis and treatment. *Chem Soc Rev*. 2018; 47: 6454-72.
167. Bankar SB, Bule MV, Singhal RS, Ananthanarayan L. Glucose oxidase—an overview. *Biotechnol Adv*. 2009; 27: 489-501.
168. Singh R, Singh S. Redox-dependent catalase mimetic cerium oxide-based nanozyme protect human hepatic cells from 3-AT induced acatalasemia. *Colloids Surf B Biointerfaces*. 2019; 175: 625-35.
169. Gao X, Feng J, Song S, Liu K, Du K, Zhou Y, et al. Tumor-targeted biocatalyst with self-accelerated cascade reactions for enhanced synergistic starvation and photodynamic therapy. *Nano Today*. 2022; 43: 101433.
170. Zhang Y, Feng S, Hu G, Fang T, Xie D, Lu Q, et al. An adenovirus-mimicking photoactive nanomachine preferentially invades and destroys cancer cells through hijacking cellular glucose metabolism. *Adv Funct Mater*. 2021; 32: 2110092.
171. Li S, Liu R, Jiang X, Qiu Y, Song X, Huang G, et al. Near-infrared light-triggered sulfur dioxide gas therapy of cancer. *ACS Nano*. 2019; 13: 2103-13.
172. Thakar SB, Ghorpade PN, Shaker B, Lee J, Na D. Gas-mediated cancer therapy combined with starvation therapy, ultrasound therapy, chemotherapy, radiotherapy, and photodynamic therapy: a review. *Environ Chem Lett*. 2021; 19: 2981-93.
173. Yu YT, Shi SW, Wang Y, Zhang QL, Gao SH, Yang SP, et al. A ruthenium nitrosyl-functionalized magnetic nanoplateform with near-Infrared light-controlled nitric oxide delivery and photothermal effect for enhanced antitumor and antibacterial therapy. *ACS Appl Mater Interfaces*. 2020; 12: 312-21.
174. Liu S, Li W, Dong S, Zhang F, Dong Y, Tian B, et al. An all-in-one theranostic nanoplateform based on upconversion dendritic mesoporous silica nanocomposites for synergistic chemodynamic/photodynamic/gas therapy. *Nanoscale*. 2020; 12: 24146-61.
175. Zhang F, Liu S, Zhang N, Kuang Y, Li W, Gai S, et al. X-ray-triggered NO-released Bi-SNO nanoparticles: all-in-one nano-radiosensitizer with photothermal/gas therapy for enhanced radiotherapy. *Nanoscale*. 2020; 12: 19293-307.
176. Ouyang J, Tang Z, Farokhzad N, Kong N, Kim NY, Feng C, et al. Ultrasound mediated therapy: Recent progress and challenges in nanoscience. *Nano Today*. 2020; 35: 100949.
177. Fu J, Li T, Zhu Y, Hao Y. Ultrasound-activated oxygen and ROS generation nanosystem systematically modulates tumor microenvironment and sensitizes sonodynamic therapy for hypoxic solid tumors. *Adv Funct Mater*. 2019; 29: 1906195.
178. Qian X, Zheng Y, Chen Y. Micro/nanoparticle-augmented sonodynamic therapy (SDT): Breaking the depth shallow of photoactivation. *Adv Mater*. 2016; 28: 8097-129.
179. Pan X, Bai L, Wang H, Wu Q, Wang H, Liu S, et al. Metal-organic-framework-derived carbon nanostructure augmented sonodynamic cancer therapy. *Adv Mater*. 2018; 30: 1800180.
180. Chen M, Liang X, Gao C, Zhao R, Zhang N, Wang S, et al. Ultrasound triggered conversion of porphyrin/camptothecin-fluorouracil triad microbubbles into nanoparticles overcomes multidrug resistance in colorectal cancer. *ACS Nano*. 2018; 12: 7312-26.
181. Zhang Y, Zhang X, Yang H, Yu L, Xu Y, Sharma A, et al. Advanced biotechnology-assisted precise sonodynamic therapy. *Chem Soc Rev*. 2021; 50: 11227-48.
182. Cao Y, Wu T, Dai W, Dong H, Zhang X. TiO₂ Nanosheets with the Au nanocrystal-decorated edge for mitochondria-targeting enhanced sonodynamic therapy. *Chem Mater*. 2019; 31: 9105-14.
183. Cheng K, Zhang RY, Yang XQ, Zhang XS, Zhang F, An J, et al. One-for-all nanoplateform for synergistic mild cascade-potentiated ultrasound therapy induced with targeting imaging-guided photothermal therapy. *ACS Appl Mater Interfaces*. 2020; 12: 40052-66.
184. Shi S, Li D, Li Y, Feng Z, Du Y, Nie Y. LncRNA CR749391 acts as a tumor suppressor to upregulate KLF6 expression via interacting with miR-181a in gastric cancer. *Exp Ther Med*. 2020; 19: 569-78.
185. Yan L, Zhang Y, Li K, Wang M, Li J, Qi Z, et al. miR-593-5p inhibit cell proliferation by targeting PLK1 in non small cell lung cancer cells. *Pathol Res Pract*. 2020; 216: 152786.
186. Qian K, Zhang J, Lu J, Liu W, Yao X, Chen Q, et al. FAM172A modulates apoptosis and proliferation of colon cancer cells via STAT1 binding to its promoter. *Oncol Rep*. 2016; 35: 1273-80.
187. Kim YH, Kim KT, Lee SJ, Hong SH, Moon JY, Yoon EK, et al. Image-aided suicide gene therapy utilizing multifunctional hTERT-targeting adenovirus for clinical translation in hepatocellular carcinoma. *Theranostics*. 2016; 6: 357-68.
188. Ye L, Chen Y, Mao J, Lei X, Yang Q, Cui C. Dendrimer-modified gold nanorods as a platform for combinational gene therapy and photothermal therapy of tumors. *J Exp Clin Cancer Res*. 2021; 40: 303.
189. Chen Z, Guo W, Wu Q, Tan L, Ma T, Fu C, et al. Tumor reoxygenation for enhanced combination of radiation therapy and microwave thermal therapy using oxygen generation in situ by CuO nanosuperparticles under microwave irradiation. *Theranostics*. 2020; 10: 4659-75.
190. Chen Z, Niu M, Chen G, Wu Q, Tan L, Fu C, et al. Oxygen production of modified core-shell CuO@ZrO₂ nanocomposites by microwave radiation to alleviate cancer hypoxia for enhanced chemo-microwave thermal therapy. *ACS Nano*. 2018; 12: 12721-32.
191. Fu Q, Zhang X, Song J, Yang H. Plasmonic gold nanoagents for cancer imaging and therapy. *View*. 2021; 2: 20200149.